ACSNANO

www.acsnano.org

ARTICLE

Antiangiogenic Therapeutic mRNA Delivery Using Lung-Selective Polymeric Nanomedicine for Lung Cancer Treatment

Ngoc Duy Le, Bao Loc Nguyen, Basavaraj Rudragouda Patil, HeeSang Chun, SiYoon Kim, Thi Oanh Oanh Nguyen, Sunil Mishra, Sudarshan Tandukar, Jae-Hoon Chang, Dong Young Kim, Sung Giu Jin, Han-Gon Choi, Sae Kwang Ku, Jeonghwan Kim,* and Jong Oh Kim*

Cite This: *ACS Nano* 2024, 18, 8392−8410

Read Online

ACCESS | Metrics & More | Article Recommendations | Supporting Information

ABSTRACT: Therapeutic antibodies that block vascular endothelial growth factor (VEGF) show clinical benefits in treating nonsmall cell lung cancers (NSCLCs) by inhibiting tumor angiogenesis. Nonetheless, the therapeutic effects of systemically administered anti-VEGF antibodies are often hindered in NSCLCs because of their limited distribution in the lungs and their adverse effects on normal tissues. These challenges can be overcome by delivering therapeutic antibodies in their mRNA form to lung endothelial cells, a primary target of VEGF-mediated pulmonary angiogenesis, to suppress the NSCLCs. In this study, we synthesized derivatives of poly(β-amino esters) (PBAEs) and prepared nanoparticles to encapsulate the synthetic mRNA encoding bevacizumab, an anti-VEGF antibody used in the clinic. Optimization of nanoparticle formulations resulted in a selective lung transfection after intravenous administration. Notably, the optimized PBAE nanoparticles were distributed in lung endothelial cells, resulting in the secretion of bevacizumab. We analyzed the protein corona on the lung- and spleen-targeting nanoparticles using proteomics and found distinctive features potentially contributing to their organ-selectivity. Lastly, bevacizumab mRNA delivered by the lung-targeting PBAE nanoparticles more significantly inhibited tumor proliferation and angiogenesis than recombinant bevacizumab protein in orthotopic NSCLC mouse models, supporting the therapeutic potential of bevacizumab mRNA therapy and its selective delivery through lung-targeting nanoparticles. Our proof-of-principle results highlight the clinical benefits of nanoparticle-mediated mRNA therapy in anticancer antibody treatment in preclinical models.

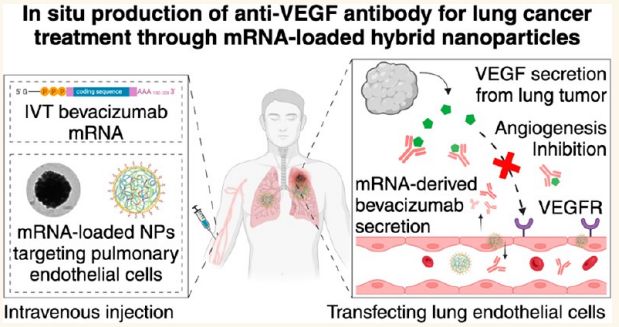

KEYWORDS: *Bevacizumab, Poly(β-amino ester), Nanoparticles, Angiogenesis, Nonsmall cell lung cancer, Lung targeting*

INTRODUCTION

Tumor angiogenesis, the rapid proliferation of new blood vessels, plays a vital role in tumor growth, invasion, and metastasis. The microenvironment of growing solid tumors is deprived of oxygen and nutrients, resulting in metabolic transformation and the expression of glycolysis-related proteins and epithelial-mesenchymal transition.[1,2] Such tumor reprogramming also involves various vascular endothelial-derived growth factor (VEGF) pathways, which are key mediators of vascularization, such as the upregulation of VEGF or its receptor expression.[3] Although VEGF is responsible for physiological development and homeostasis, its implications in tumor pathogenesis are primarily associated with its influence on vascular permeability and neoangiogenesis. Diverse strategies have been explored to block VEGF pathways in tumors, and some have shown efficacy in inhibiting tumor growth. Bevacizumab (Avastin, Roche) is the anti-VEGF antibody approved by the U.S. FDA in 2004 for cancer treatment. Its current applications include colorectal, ovarian, and nonsmall-cell lung cancers (NSCLCs).[4] Despite its excellent tumor-suppressing efficacy, its distribution is often limited to the vascular and interstitial spaces, diminishing its clinical benefits in other organs and tissues.[5] A study revealed that approximately

Received: December 25, 2023
Revised: February 23, 2024
Accepted: March 4, 2024
Published: March 7, 2024

https://doi.org/10.1021/acsnano.3c13039
ACS Nano 2024, 18, 8392−8410

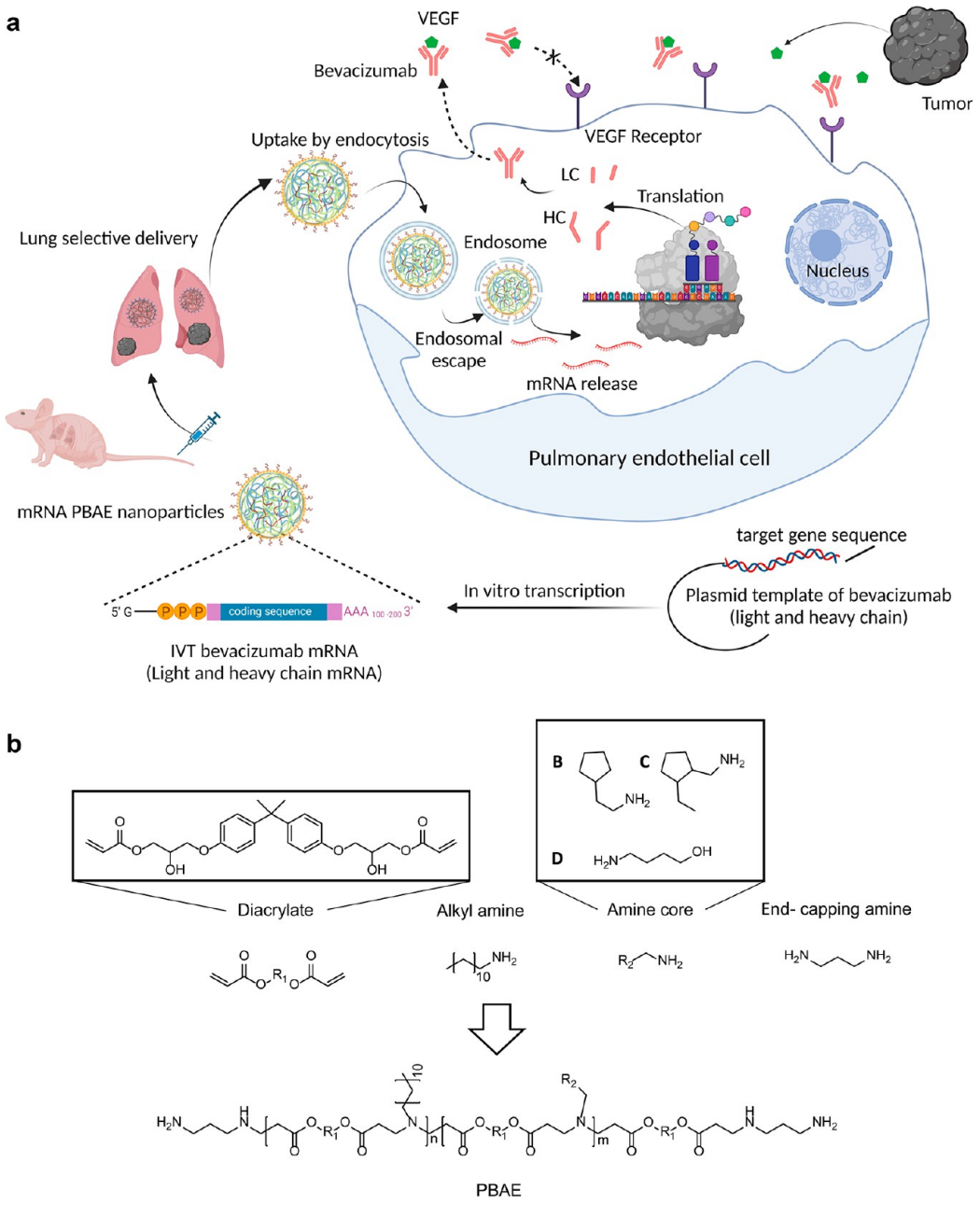

Figure 1. (a) Schematic illustration of the hypothetical mechanism of action of PBAE NP-delivered bevacizumab mRNA therapy in the treatment of NSCLCs. The mRNA transcripts encoding bevacizumab's heavy and light chains were synthesized and encapsulated in the PBAE NPs. The NPs were intravenously administered and selectively distributed to the PECs. mRNA transfection led to the production and secretion of bevacizumab antibody in the lungs, and the antibody stopped the lung tumor-derived VEGF from binding to VEGF receptors, inhibiting tumor angiogenesis (created by BioRender). (b) Library of PBAE polymers synthesized and used in this study.

1% of the radiolabeled bevacizumab reached the human lungs following systemic administration, suggesting the limited biodistribution to the tumors.[6] Because healthy tissues require VEGF for homeostasis and vascular development, bevacizumab-mediated VEGF inhibition in normal tissues can cause endothelial cell dysfunction or the regression of fenestrated capillaries.[7] Therefore, unmet needs exist to inhibit tumor-selective VEGF and suppress tumor angiogenesis.

The recent success of mRNA vaccines in the clinic has given rise to much interest in using mRNA for treatment.[8,9] Several preclinical studies showed the potential of anticancer mRNA therapy by expressing tumor antigens,[10] CD40,[11] OX40,[12] or interleukin-12.[13] Especially, because of mRNA's capability of producing virtually any protein, it has drawn attention to the development of therapeutic antibodies for cancer treatment.[14] Using mRNA as a platform for monoclonal antibody delivery uses transfected cells to produce therapeutic antibodies. This is attractive because of the straightforward, low-cost, and scalable characteristics of mRNA therapeutics. Therefore, bevacizumab-encoded mRNA could be a great alternative to the bevacizumab protein. In addition, using target-specific nanoparticles (NPs), bevacizumab mRNA can be selectively delivered to targeted tumor tissues, improving the bioavailability of the antibody, blocking VEGF, and inhibiting tumor angiogenesis. In NSCLCs, pulmonary endothelial cells (PECs) are the primary cellular targets of VEGF for angiogenesis.[15] Therefore, we hypothesized

https://doi.org/10.1021/acsnano.3c13039
ACS Nano 2024, 18, 8392−8410

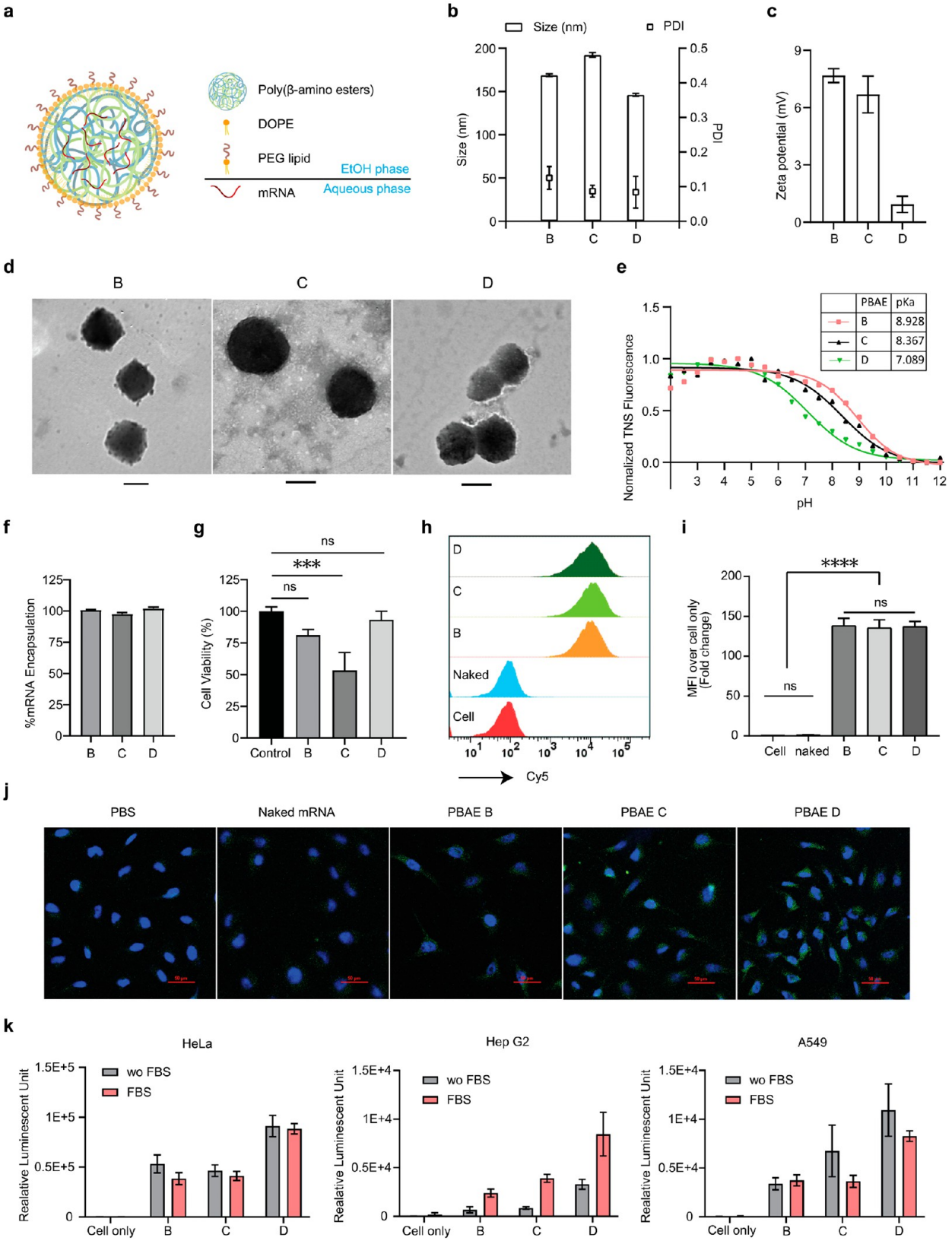

Figure 2. Characterization of physicochemical properties and *in vitro* mRNA delivery of PBAE NPs. (a) Schematic diagram of a mRNA-loaded PBAE NP. (b, c) Physicochemical properties of various PBAE-based NPs encapsulating FLuc mRNA: (b) particle size, polydispersity index (PDI), and (c) zeta potential. (d) Representative TEM images of various PBAE NPs encapsulating FLuc mRNA: PBAE-B (left), PBAE-C (middle), and PBAE-D (right). Scale bars indicate 100 nm. (e) Determination of apparent pK_a of various PBAE NPs encapsulating FLuc mRNA. An inset shows the calculated apparent pK_a values of the NPs. (f) FLuc mRNA encapsulation (%) of various PBAE NPs. (g) Cell viability of HeLa cells exposed to PBS or PBAE NP treatments. Data are represented as mean ± standard deviation (n = 4). Statistical analysis was performed using one-way ANOVA with Tukey's multiple comparisons test, *ns*, not significant; ***p < 0.001 (h) Cy5 histograms of the cells

https://doi.org/10.1021/acsnano.3c13039
ACS Nano 2024, 18, 8392−8410

Figure 2. continued

treated with PBS, naked mRNA, or various mRNA-loaded PBAE NPs. (i) Cellular uptake of naked mRNA and various mRNA-loaded PBAE NPs. Data are represented as mean ± standard deviation (n = 3). Statistical analysis was performed using one-way ANOVA with Tukey's multiple comparisons test, *ns*, not significant; ****p < 0.0001; (j) Confocal images of HeLa-Gal8-GFP cells treated with (left to right) PBS, naked mRNA, mRNA-loaded PBAE-B, PBAE-C, or PBAE-D based NPs. Nuclei (blue) were counterstained. (k) *In vitro* luciferase expression after PBAE NP-mediated FLuc mRNA delivery in HeLa (left), Hep G2 (middle), and A549 (right) cells in the presence (red) or absence (gray) of FBS.

that PEC-selective mRNA delivery for bevacizumab production could efficiently inhibit VEGF-mediated angiogenesis and suppress tumor growth (Figure 1a). Poly(β-amino esters) (PBAEs) are cationic, biodegradable polymers capable of delivering nucleic acids to the inside of cells *in vivo*.[16] Additionally, when combined with bioactive lipids, they preferentially transfect the lungs following systemic administration.[17,18] Taking advantage of the intrinsic lung-targeting properties of PBAE, we synthesized a small library of PBAE derivatives and optimized the formulation of PBAE-lipid hybrid NPs for lung-selective mRNA delivery (Figure 1a). Our results suggest that mRNA-based therapeutic antibody delivery could be a promising alternative for effectively inhibiting lung angiogenesis at the site of vascularization and eradicating NSCLCs.

RESULTS AND DISCUSSION

We chose PBAE NPs as the delivery vectors of mRNA to the pulmonary system. First, a small library of PBAEs was synthesized via Michael addition using bisphenol A glycerolate diacrylate, hydrophilic amines (B, C, or D), and dodecylamine. The polymers were then end-capped with monomer 1,3-diaminopropane, resulting in PBAE-B, -C, and -D (Figure 1b). ^{1}H NMR was used to characterize the PBAE polymers (Figures S1−S3). The aromatic protons of the diacrylate were observed at 6.80 and 7.10 ppm. The disappearance of diacrylate proton signals at 5.36, 5.96, 6.20, and 6.23 ppm indicated polymerization by aza-Michael addition (Figures S1−S4).

Using these PBAE polymers, we prepared PBAE-lipid hybrid NPs containing dioleoylphosphatidylethanolamine (DOPE) and DMG-PEG$_{2K}$ for mRNA delivery. PBAE polymers and lipids were dissolved in ethanol in a predetermined ratio (PBAE:DOPE:DMG-PEG$_{2K}$ = 45:3:2.75, w/w), and mRNA was prepared in an acidic aqueous phase. The vigorous mixing of the two phases led to the self-assembly of PBAE-lipid hybrid NPs containing mRNA (Figure 2a). All three PBAE NPs were 100−200 nm in hydrodynamic diameter with narrow distributions (polydispersity indexes (PDI) < 0.2; Figure 2b). Their zeta potentials ranged from 1 to 10 mV, suggesting a neutral surface charge on the PBAE NPs (Figure 2c). The morphology of the PBAE NPs was further characterized using transmission electron microscopy (TEM). TEM imaging revealed that the PBAE NPs were spherical in shape and 100−200 nm in size (Figure 2d). To determine the apparent pK_a of PBAE NPs, 2-(p-toluidino)-6-naphthalene sulfonic acid (TNS) assays were performed. The fluorescence intensity of TNS from the PBAE NPs showed sigmoidal curves in response to varying pH conditions, and the apparent pK_a values of the NPs containing PBAE-B, -C, and -D were 8.9, 8.3, and 7.08, respectively (Figure 2e), which seemed to correlate with the zeta potentials of the NPs (Figure 2c). All PBAE NPs showed high levels of mRNA encapsulation (>95%; Figure 2f).

After the physicochemical properties of the PBAE NPs were confirmed, their *in vitro* cytotoxicity was studied. When tested in HeLa cells, PBAE-B and -D NPs treatment did not decrease cell viability, while cell viability was significantly reduced by PBAE-C NPs treatment (Figure 2g). In the subsequent test on human umbilical vein endothelial cells (HUVECs), PBAE-B and -C treatment led to pronounced or mild decreases in cell viabilities, respectively, while PBAE-D NPs did not reduce cell viability (Figure S5a). The *in vitro* cellular uptake of the PBAE NPs containing Cy5-labeled mRNA was assessed by using flow cytometry. All three PBAE NPs efficiently entered both HeLa cells and HUVECs, while naked mRNA failed to enter (Figures 2h,i, S5b, and S5c). Next, the endosomal disruption of PBAE NPs was studied using galectin 8 (Gal8) recruitment assays.[19,20] Endosomal escape is an integral stage for NPs to achieve intracellular delivery of nucleic acids. Treatment of Gal8-green fluorescent protein (GFP) reporter cells with PBAE NPs led to various levels of GFP recruitment, suggesting different efficiencies of the NPs for endosomal escape (Figures 2j and S6). Compared with the phosphate buffered saline (PBS) treatment, the PBAE NP treatment increased the number of GFP puncta in reporter cells. In particular, the NPs of PBAE-C and PBAE-D led to GFP recruitment that was greater than that of PBAE-B. The various levels of GFP recruitment caused by the PBAE NP treatment may result from the different pK_a values of the NPs. PBAE-D NPs with relatively lower pK_a values are more likely to be rapidly ionized at the endosomal pH than the other two NPs, possibly having a higher chance of disrupting the endosomal membrane.[21] Naked mRNA treatment did not change the level of GFP recruitment, which likely resulted from a failed cellular entry. *In vitro* mRNA transfection in various cell lines was performed, and in all of the cell lines tested (HeLa, Hep G2, A549, and HUVEC), the NPs containing PBAE-D showed the highest luciferase expression among the three NPs (Figures 2k and S7). Depletion of fetal bovine serum (FBS) did not change NP-mediated mRNA transfection in HeLa cells but affected Hep G2 and A549 cells. Interestingly, Hep G2 cells were more amenable to NP-assisted mRNA delivery in the presence of FBS, whereas A549 and HUVECs showed only moderate increases in the level of luciferase expression when FBS was depleted (Figure 2k). This could be because the NPs complexed with serum proteins were processed differently, depending on the origin of the cell lines. Based on the *in vitro* screening results, PBAE-D was selected as a suitable polymer for mRNA delivery and further optimized in the formulations.

To optimize the PBAE-D-based NP formulation, a library with various polymer/lipid ratios (Table S1) was prepared. In addition, two other poly(ethylene glycol) (PEG)-anchored lipids, DMG-PEG$_{2K}$ and DSPE-PEG$_{2K}$ were also included. With the PEG molarity fixed in formulations (F1−F6, Table S1), all NPs had sizes of less than 250 nm (Figure 3a). The inclusion of DSPE-PEG$_{2K}$ decreased the particle size compared to that of DMG-PEG$_{2K}$, which could result from their different lipid tail lengths (C14:0 DMG-PEG$_{2K}$ and C18:0 DSPE-PEG$_{2K}$). The level of mRNA encapsulation increased proportionally with the amount of PBAE-D in the formulations because of the number

https://doi.org/10.1021/acsnano.3c13039
ACS Nano 2024, 18, 8392−8410

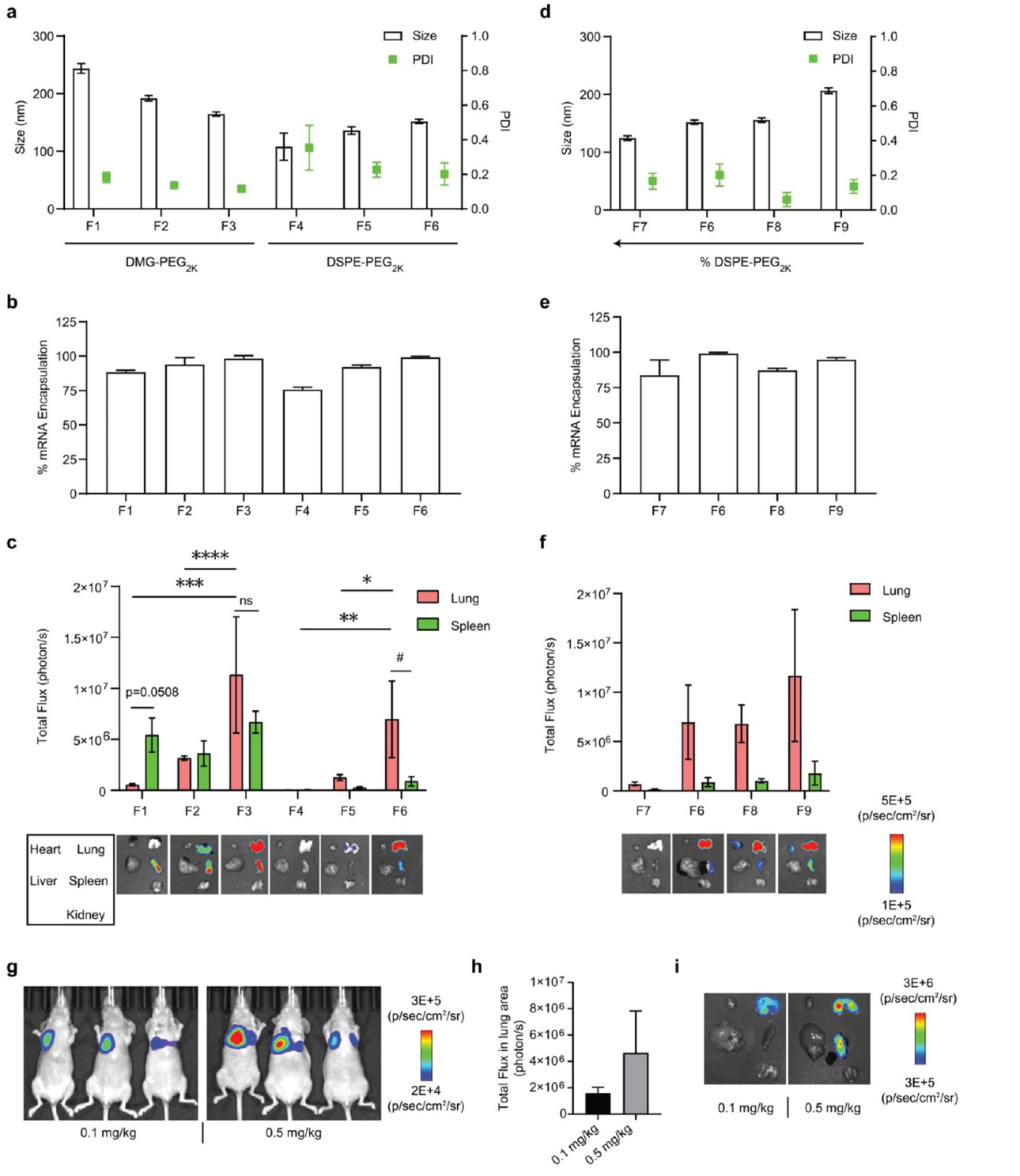

Figure 3. Characterization and optimization of PBAE-D-based NPs. (a, b) Physicochemical properties of PBAE-D-based formulations F1−F6 encapsulating FLuc mRNA: (a) particle size, polydispersity index (PDI) and (b) mRNA encapsulation. (c). *Ex vivo* bioluminescence of major organs of BALB/c mice that received an IV injection of F1−F6 encapsulating FLuc mRNA (0.1 mg/kg). Data are represented as mean ± standard deviation (n = 3). The difference between FLuc expression in the lungs and the spleen of each formulation was analyzed by two-way ANOVA with Sidak's multiple comparisons test, ns, not significant, $^{\#}p < 0.05$. Two-way ANOVA with Tukey's multiple comparisons test was used to compare FLuc expression in the lungs or spleen of various formulations, $*p < 0.05$, $**p < 0.01$; $***p < 0.001$; $****p < 0.0001$. (d, e) Physicochemical properties of PBAE-D based formulations F6−F9 encapsulating FLuc mRNA: (d) Particle size, polydispersity index (PDI), and (e) mRNA encapsulation. (f) *Ex vivo* bioluminescence of major organs of BALB/c mice that received an IV injection of F6−F9 encapsulating FLuc mRNA (0.1 mg/kg). (g−i) Characterization of *in vivo* mRNA transfection by F6 NPs encapsulating FLuc mRNA in BALB/c nude mice. (g) *In vivo* luciferase expression, (h) Counted total flux in the lung areas and (i) *ex vivo* luciferase expression in the major organs of BALB/c nude mice that received an IV injection of F6 NPs encapsulating FLuc mRNA at dose of 0.1 or 0.5 mg mRNA/kg. Data are represented as mean ± standard deviation (n = 3).

https://doi.org/10.1021/acsnano.3c13039
ACS Nano 2024, 18, 8392−8410

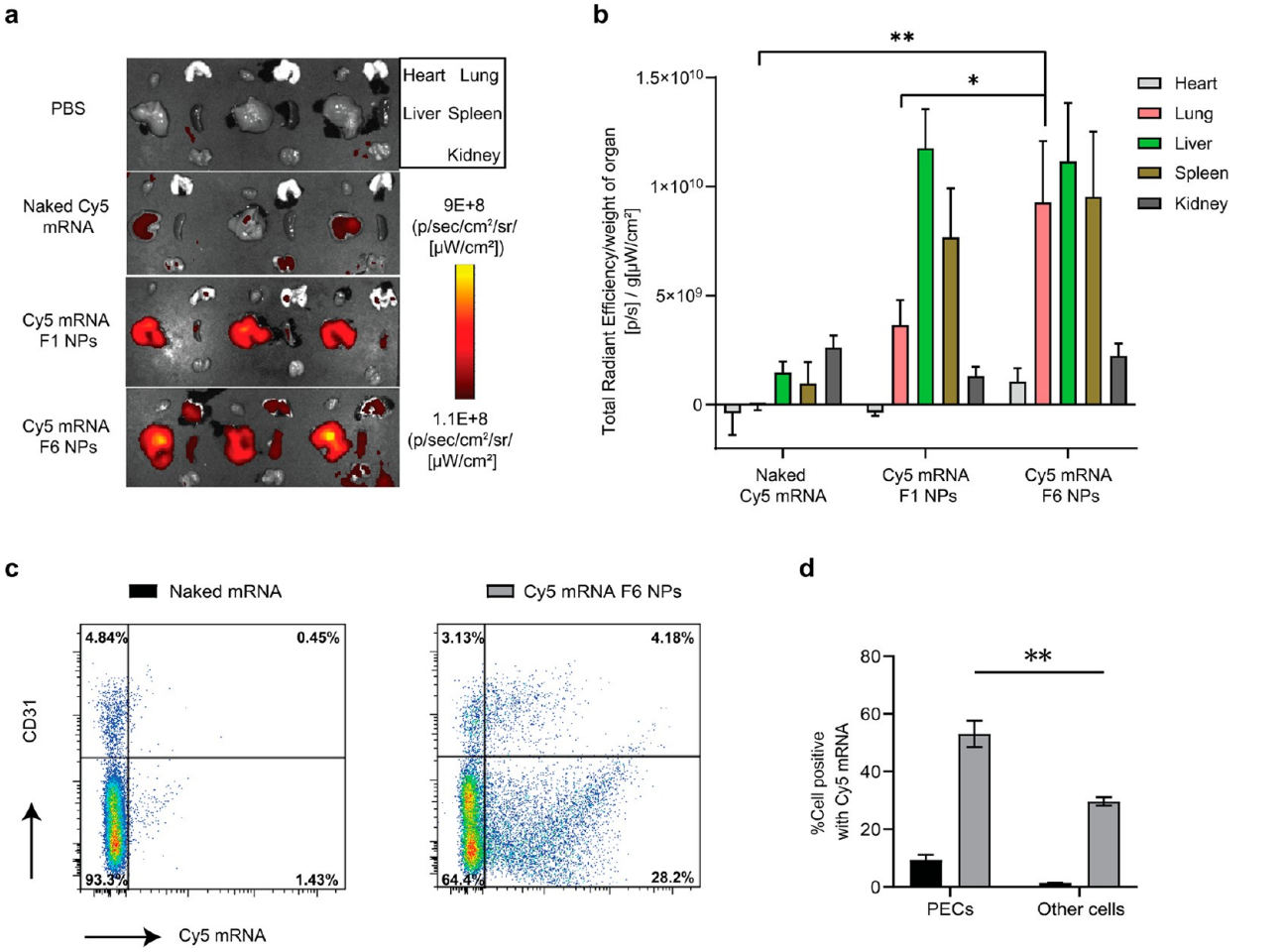

Figure 4. Biodistribution and PEC uptake of PBAE NPs containing Cy5-labeled mRNA. (a) Cy5 fluorescent images of the major organs from BALB/c mice treated with PBS, naked Cy5 mRNA, F1 and F6 NPs encapsulating Cy5 mRNA at 4 h postinjection. (b) Normalized Cy5 signals in the major organs. Data are presented as mean ± standard deviation ($n = 3$). Two-tailed Student *t*-test, $^{*}p < 0.05$, $^{**}p < 0.01$. (c) Flow cytometric analysis of the PECs uptake of Cy5 mRNA: naked mRNA (left) and F6 NP-delivered mRNA (right). (d) Cell type analysis of pulmonary cells exhibiting Cy5 signals from the delivered mRNA: naked mRNA (black) and F6 NP-delivered mRNA (gray). Data are represented as mean ± standard deviation ($n = 3$). Two-tailed Student's *t* test, $^{**}p < 0.01$.

of amine groups available for mRNA complexation (Figure 3b). When administered intravenously, PBAE NP-mediated luciferase expression was observed in the spleen and lungs, as shown previously (Figures 3c and S8).[18] It was shown that the increasing amount of PBAE-D in NPs seemed to produce greater luciferase expression *in vivo*, especially in the lungs (Figure 3c). In addition, the NPs having DMG-PEG_{2K} produced greater mRNA transfection *in vivo* than the NPs having DSPE-PEG_{2K}, likely resulting from the rapid PEG shedding of DMG-PEG_{2K}.[22] Out of six formulations, F3 and F6 showed greater levels of mRNA transfection *in vivo* than the others. Although F3 produced the highest lung luciferase expression, F6 led to more selective lung transfection than spleen transfection (Figure 3c). Based on the lung selectivity of F6, the formulation library was expanded to screen the effects of the amount of DSPE-PEG_{2K} (F6–F9, Table S1). The resulting NPs decreased in size in response to increasing PEG content (Figure 3d), and all NPs showed good mRNA encapsulation (>80%) (Figure 3e). Following the systemic administration of NPs, bioluminescence was found primarily in the lungs and marginally in the spleen (Figures 3f and S8). Increasing PEG content in the PBAE NPs reduced luciferase expression *in vivo*, possibly because the dense PEG layer inhibited interactions with serum proteins.[22] Although changes in the amount of DSPE-PEG_{2K} resulted in a significant change in total firefly luciferase (FLuc) expression, the percentages of FLuc expression in the lungs were similar in all F6–F9 formulations (Figure S9). The F9 NPs showed the highest lung luciferase expression; however, their sizes were larger than 200 nm. Both F6 and F8 NPs were approximately 150 nm in size and produced good and selective luciferase expression in the lungs; however, F6 NPs encapsulated mRNA more efficiently than F8 NPs (Figure 3d–f). Therefore, we continued to explore therapeutic mRNA delivery using F6 NPs. F6-mediated mRNA transfection in immunodeficient mice was examined and exhibited a dose-dependent increase in protein production (Figure 3g,h). In addition, the dose-dependent lung transfection of mRNA was also confirmed in immunodeficient mice by using F6 NPs (Figure 3i).

To characterize the biodistribution of F1 and F6, the fluorescence signals of Cy5-labeled mRNA encapsulated in the NPs were measured. Cy5 signals derived from F6 were distributed in the liver, lungs, and spleen, while signals from F1 were found in the liver and marginally in the spleen (Figure 4a). Cy5 signals from naked mRNA were detected in the liver and kidneys. When the Cy5 signals were normalized to the weight of each organ, the lungs, liver, and spleen displayed

https://doi.org/10.1021/acsnano.3c13039
ACS Nano 2024, 18, 8392–8410

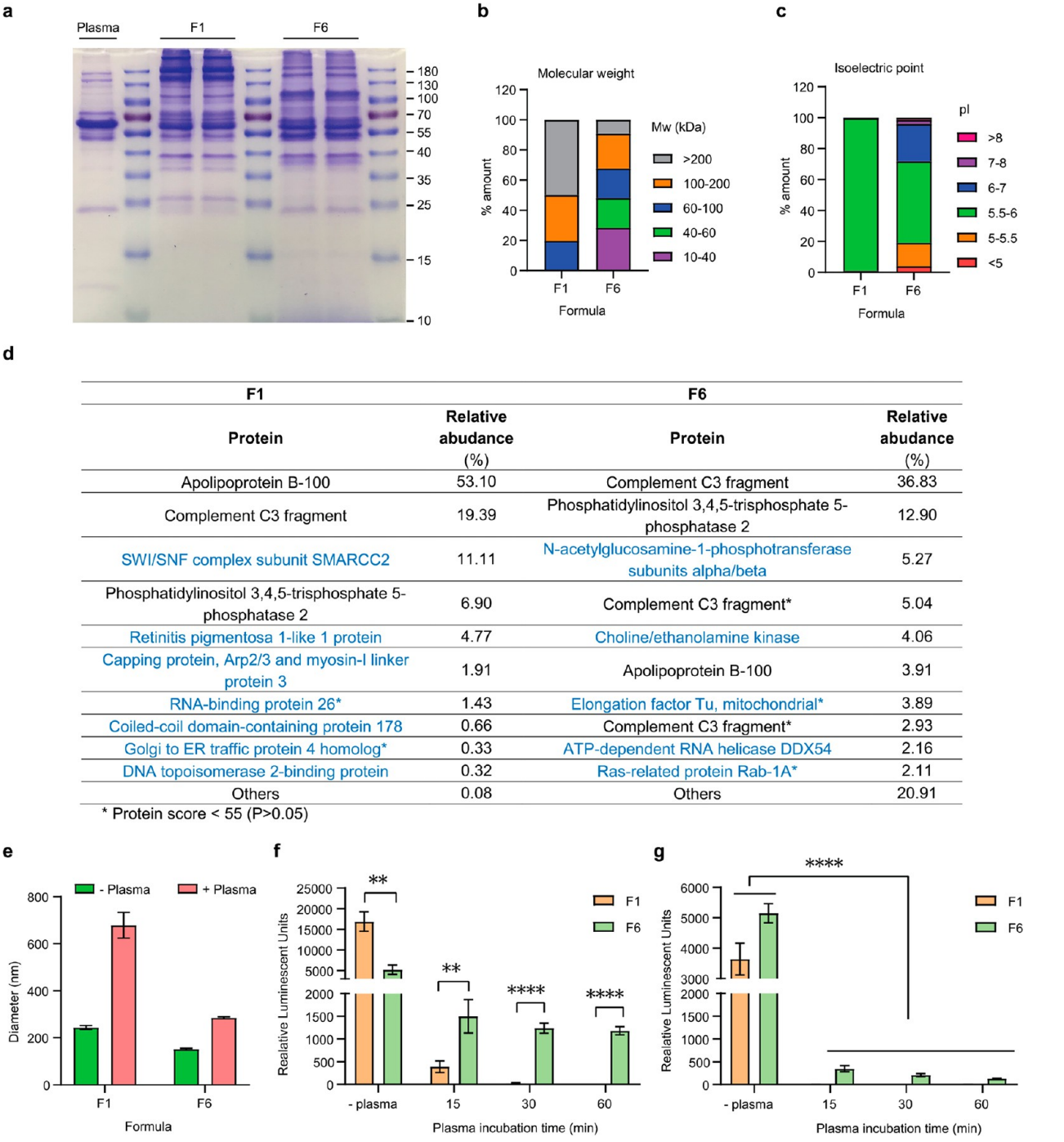

d

F1		F6	
Protein	Relative abudance (%)	Protein	Relative abudance (%)
Apolipoprotein B-100	53.10	Complement C3 fragment	36.83
Complement C3 fragment	19.39	Phosphatidylinositol 3,4,5-trisphosphate 5-phosphatase 2	12.90
SWI/SNF complex subunit SMARCC2	11.11	N-acetylglucosamine-1-phosphotransferase subunits alpha/beta	5.27
Phosphatidylinositol 3,4,5-trisphosphate 5-phosphatase 2	6.90	Complement C3 fragment*	5.04
Retinitis pigmentosa 1-like 1 protein	4.77	Choline/ethanolamine kinase	4.06
Capping protein, Arp2/3 and myosin-I linker protein 3	1.91	Apolipoprotein B-100	3.91
RNA-binding protein 26*	1.43	Elongation factor Tu, mitochondrial*	3.89
Coiled-coil domain-containing protein 178	0.66	Complement C3 fragment*	2.93
Golgi to ER traffic protein 4 homolog*	0.33	ATP-dependent RNA helicase DDX54	2.16
DNA topoisomerase 2-binding protein	0.32	Ras-related protein Rab-1A*	2.11
Others	0.08	Others	20.91

* Protein score < 55 (P>0.05)

Figure 5. Characterization of the interactions between F1 and F6 NPs and plasma proteins. (a) 1D SDS-PAGE analysis of the protein samples collected from mouse plasma or the surface of plasma-incubated NPs. (b, c) Proteins extracted from the NP surface were subjected to 2D SDS-PAGE and categorized based on their (b) molecular weight and (c) isoelectric point. (d) The top 10 most abundant proteins in the protein coronas on the NP surfaces. The proteins distinctive to the protein corona of each formulation were indicated by a blue color. (e) Particle size of NPs containing FLuc mRNA following incubation with plasma at 37 °C for 1 h. (f, g) *In vitro* luciferase expression of (f) HUVECs and (g) Hep G2 cells treated with plasma-incubated or nonincubated NPs containing FLuc mRNA. Data are presented as mean ± standard deviation ($n = 3$). Statistical analysis was conducted using a two-tailed Student's *t* test for HUVEC results and one-way ANOVA with Dunnett's multiple comparisons test for Hep G2 cells. **$p < 0.01$, ****$p < 0.0001$.

comparable fluorescence levels, indicating the biodistribution of F6 NPs to these organs (Figure 4b). Specifically, F6 NPs exhibited a significantly greater accumulation in the lungs than did F1 NPs. Further, the cell-specific distribution of the NPs was explored using flow cytometry (Figure S10). Approximately 31.0% of the total lung cells were Cy5-positive when mRNA was systemically administered by using F6 NPs (Figure 4c). In particular, the Cy5 signal was detected in approximately 53.1% of the PECs. In comparison, it was only approximately 29.6% in other lung cells (Figure 4d), suggesting the preferential distribution of F6 NPs to PECs, which could be advantageous for delivering anticancer therapeutic mRNA for the treatment of

https://doi.org/10.1021/acsnano.3c13039
ACS Nano 2024, 18, 8392−8410

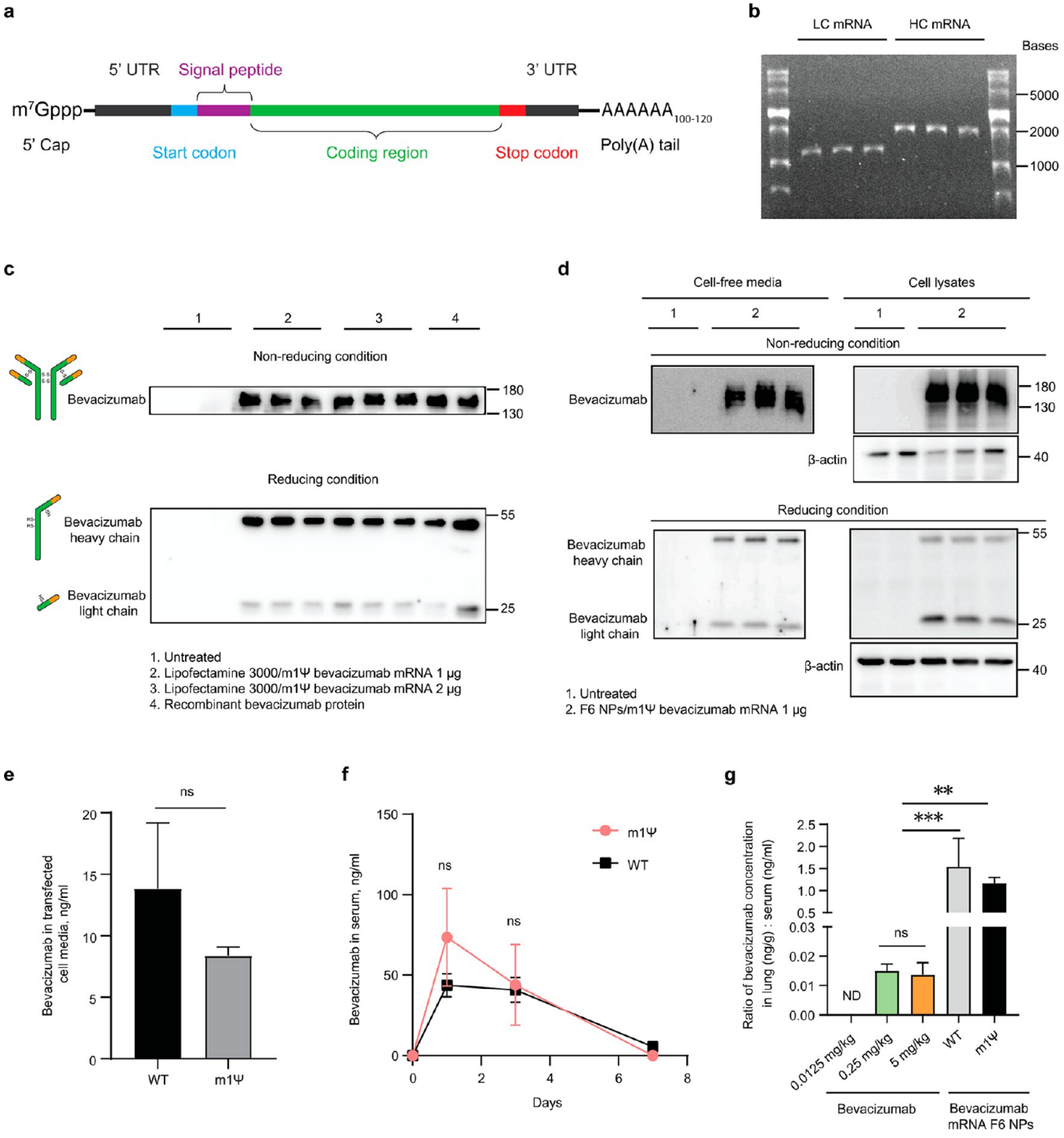

Figure 6. Bevacizumab mRNA delivery using F6 NPs. (a) A schematic illustration of *in vitro* transcribed bevacizumab mRNA. (b) Agarose gel electrophoresis of the mRNA transcripts encoding light chain (LC) and heavy chain (HC) of bevacizumab. (c) Western blot analysis of bevacizumab in the conditioned media of HeLa cells after mRNA transfection using lipofectamine 3000, with recombinant bevacizumab protein as a positive control. (d) Western blot analysis of bevacizumab in the conditioned media (left) and the cell lysate (right) of A549 cells after bevacizumab mRNA transfection using F6. (e) Quantification of bevacizumab in the conditioned media 24 h after F6-mediated mRNA transfection of HeLa cells (125 ng mRNA/well). mRNA was synthesized using WT (black) or modified (m1Ψ) nucleotides (gray). Data are presented as mean ± standard deviation ($n = 3$). Statistical analysis was performed using a two-tailed Student's *t* test, *ns*; not significant. (f) Time-dependent serum concentrations of bevacizumab in mice after intravenous administration of F6 carrying WT or m1Ψ bevacizumab mRNA (0.5 mg/kg). Data are presented as mean ± standard deviation ($n = 3$). Statistical analysis was performed using a two-tailed Student's *t* test, ns, not significant. (g) The ratios of bevacizumab concentrations in lung lysates and those in serum following the administration of various bevacizumab treatments: recombinant bevacizumab ($n = 4$) or bevacizumab mRNA loaded into F6, prepared with WT ($n = 4$) or m1Ψ nucleotides ($n = 3$). Recombinant protein was given intraperitoneally at various doses, and mRNA-loaded F6 was given intravenously at a dose of 0.5 mg/kg. Data are presented as mean ± standard deviation. Statistical analysis was performed using one-way ANOVA with Tukey's multiple comparisons test, $^{**}p < 0.01$; $^{***}p < 0.001$; *ns*, not significant, ND, not detected.

https://doi.org/10.1021/acsnano.3c13039
ACS Nano 2024, 18, 8392−8410

lung cancers. Intravenous (IV) administration of naked mRNA resulted in poor distribution in lung cells (Figure 4c,d).

To uncover the mechanism enabling the organ-selective accumulation of PBAE NPs, we studied the interactions between NPs and plasma proteins. Accumulating publications have indicated the implications of the protein corona for NP distribution *in vivo*.[23−30] Since neither F1 nor F6 contains targeting ligands, we hypothesized that the distinctive patterns of NP distribution would stem from the differential composition of the protein corona (Figure S11). After F1 and F6 were exposed to mouse plasma *ex vivo*, we isolated the associated plasma proteins by centrifugation. Sodium dodecyl sulfate-polyacrylamide gel electrophoresis (SDS-PAGE) analysis revealed that the constitutions of the protein coronas were strikingly different (Figure 5a). Specifically, the protein corona of F1 exhibited enrichment above 140 kDa, whereas F6 showed a high enrichment of bands near 60 kDa. This suggests that the surfaces of two NPs developed distinctive protein coronas. For more in-depth analysis, the isolated protein complexes were subjected to two-dimensional (2D) gel electrophoresis to separate proteins based on their isoelectric point (pI) and molecular weight. When classified according to molecular weight, it was observed that proteins with higher molecular weights were more abundant on the surface of F1, where 50% of the proteins had a molecular weight greater than 200 kDa (Figure 5b). In contrast, on the surface of F6, the molecular weight of 90% of the enriched proteins was less than 200 kDa. Furthermore, when categorized based on pI, it was established that the pI values of proteins enriched on the surface of F6 fell within the range of 5 and 7 (Figure 5c). Conversely, the pI values of proteins present on the surface of F1 were predominantly within the range 5.5 to 6. Interestingly, these physicochemical traits of proteins found on the surface of F6 correspond closely with findings from a prior publication on lung-selective lipid nanoparticles (LNPs).[30] This suggests that the pI value and molecular weight of proteins on the NP surface may have significant implications for lung transfection. Next, we proceeded to identify the ten most abundant proteins among the separated proteins through peptide mass fingerprinting. In the top ten most abundant proteins for each formulation, F1 and F6 exhibited an overlap of only three proteins, demonstrating the distinctive formation of a protein corona on each NP formulation (Figure 5d). Apolipoprotein B-100 (ApoB-100) was predominantly detected (>50%) in the protein corona of F1. Considering that the molecular mass of ApoB-100 exceeds 500 kDa, its robust binding to F1 would increase the size of protein-NP complexes. Furthermore, earlier studies showed that this binding perturbs the folding and aggregation of Apo-B100, potentially improving recognition by CD36, a receptor highly expressed in splenic macrophages.[31,32] Both F1 and F6 exhibited abundance in complement C3 fragments. C3 is recognized for its association with platelet activation, possibly interacting with P-selectin or the A3 domain of von Willebrand Factor present on the PEC surface.[33,34] However, the association of C3 with NPs also suggests the initiation of opsonization and subsequent phagocytic clearance.[35,36] The occurrence of phosphatidylinositol 3,4,5-trisphosphate 5-phosphatase 2, an enzyme responsible for lipid hydrolysis, in the protein coronas is likely attributed to the lipid components in NPs (Figure 5d). The specific enrichment of choline/ethanolamine kinase exclusively in the protein corona of F6 probably originates from an ethanolamine residue in DSPE-PEG_{2K}, which is a component not present in F1. Proteins not native to the bloodstream might be introduced due to the invasive nature of the plasma collection procedure.[37] Notably, neither apolipoprotein E nor albumin, the two blood proteins typically enriched on the LNP surface,[29] were identified in the proteomic analysis of the two PBAE NPs. This finding may support the poor liver transfection observed in both F1 and F6 (Figure 3c), suggesting that these PBAE NPs likely undergo distribution and uptake pathways distinct from those of LNPs. The proteomic analysis fell short of fully elucidating the mechanism behind the spleen- and lung-targeting processes of F1 and F6. However, it did reveal that the two PBAE NPs were associated with distinct sets of proteins following *ex vivo* incubation with plasma. To further explore the physicochemical changes in the plasma-incubated NPs, their hydrodynamic sizes were assessed. In comparison to F6, the size of F1 markedly increased upon plasma incubation (Figure 5e). It could be attributed to either the faster desorption of DMG-PEG_{2K} compared to DSPE-PEG_{2K}[22] or the stronger interaction between F1 and ApoB-100 (Figure 5d). This difference in NP sizes may contribute to the sites of transfection. Given that the size of interendothelial slits in the spleen ranges from 200 to 500 nm, the increased size of F1 could have facilitated interactions with spleen cells.[38,39] In contrast, the prolonged residence of the PEG layer and smaller size of F6 might have contributed to PEC transfection, facilitated by pulmonary anatomy features like a large surface area and slow blood perfusion.[40,41] The subsequent *in vitro* cell transfection assay revealed the impact of NP incubation with plasma on the mRNA delivery. Under serum-free conditions, F1 demonstrated significantly higher efficiency than F6 in delivering mRNA to HUVECs. However, plasma incubation notably hindered F1 from effectively transfecting endothelial cells (Figure 5f). Additionally, it was shown that plasma incubation significantly impeded both F1 and F6 from transfecting liver cells, Hep G2 (Figure 5g). Taken together, these results strongly support the idea that the interaction of NPs with proteins plays a crucial role in achieving cell- and organ-selective mRNA delivery.

Based on the preferential accumulation of F6 NPs in PECs, we aimed to determine whether pulmonary expression of bevacizumab was effective in treating NSCLCs. We hypothesized that F6-delivered bevacizumab mRNA could enhance the pulmonary bioavailability of bevacizumab upon transfection of PECs, thereby enhancing the suppression of VEGF-mediated angiogenesis and NSCLC development. For bevacizumab expression, two mRNA transcripts encoding the heavy chain (HC) and the light chain (LC) of bevacizumab were synthesized (Figures S12 and S13).[42] The synthesized mRNA transcripts also contained untranslated regions,[43] optimized signal peptide sequences,[44] and poly(A) tails (Figures 6a, S12, and S13). They were prepared using wild-type (WT) nucleotides or full substitution of uridine with N1-methylpseudouridine (m1Ψ) to compare the protein productions with or without chemical modification. In the agarose gel electrophoresis, the bands corresponding to LC and HC mRNA were observed at approximately 1200 and 2000 nt, respectively (Figure 6b). These sizes align with the anticipated size of each mRNA transcript. When delivered to HeLa cells using lipofectamine, Western blot analysis revealed the presence of bevacizumab HC and LC proteins in the cell lysates of singly treated cells (Figure S14a). In contrast, upon examination of the conditioned media, the HC protein band was absent, while the LC protein band was faintly detected (Figure S14b). This observation is attributed to the fact that the individual domains of the antibody require assembly into a complete quaternary structure linked via

https://doi.org/10.1021/acsnano.3c13039
ACS Nano 2024, 18, 8392−8410

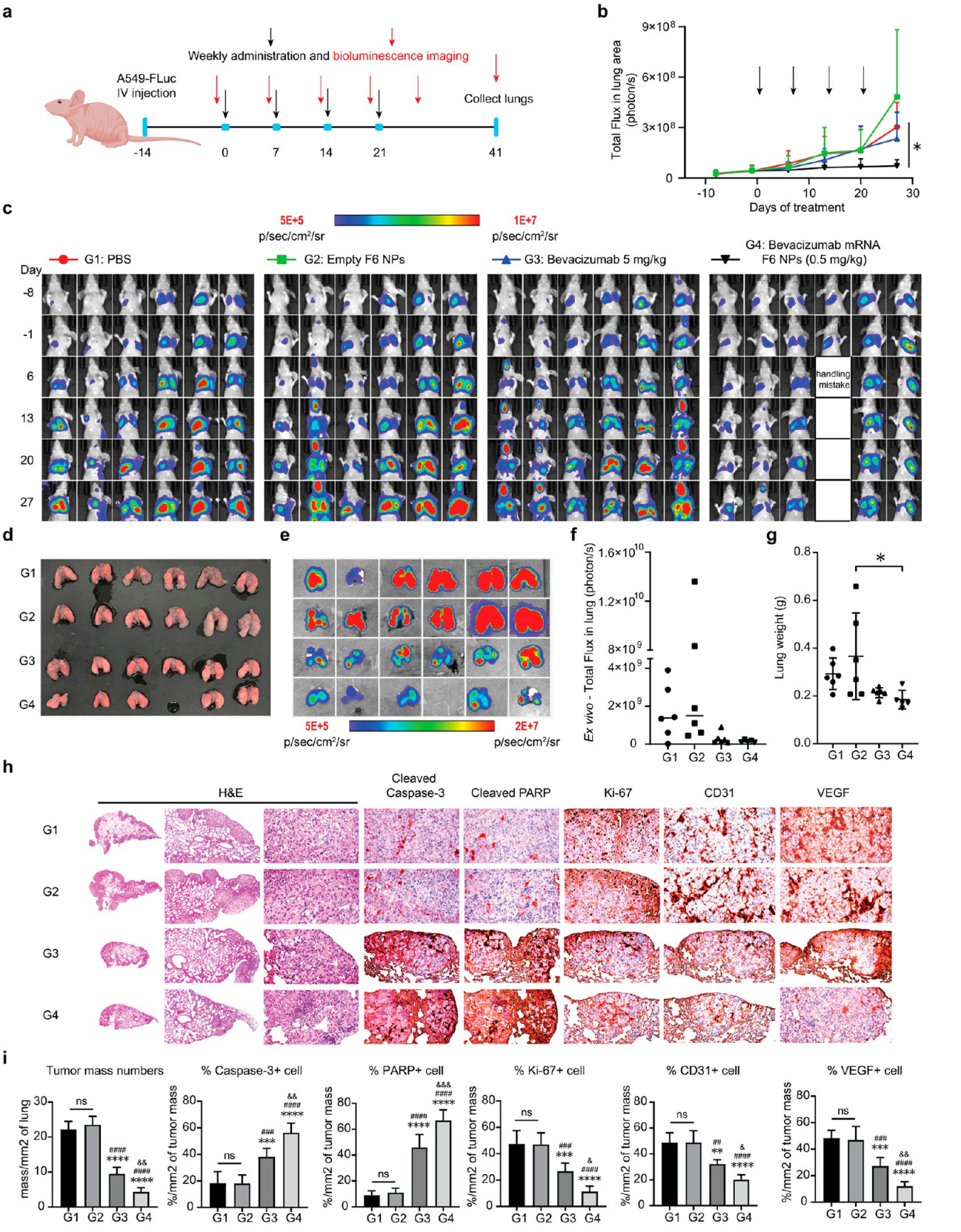

Figure 7. Antitumor activity of F6-delivered bevacizumab mRNA therapy in the orthotopic NSCLC mouse model developed by A549-FLuc IV injection. (a) Schematic diagram of dosing regimens (black arrows) and bioluminescence imaging schedules (red arrows) for treating A549-FLuc lung orthotopic tumors. (b, c) Monitored bioluminescence from the A549-FLuc lung tumors intravenously induced. (b) Quantified luciferase expression in the lungs of the mice variously treated. G1: IV injected PBS (red), G2: IV injected empty F6 NPs (green), G3: IP injected bevacizumab (blue), and G4: IV injected F6 NPs carrying bevacizumab mRNA (black). Data are represented as mean ± standard deviation (G1, G2, G3, $n = 6$; G4, $n = 5$). Statistical analysis was performed using a two-way ANOVA with Tukey's multiple comparisons test, *p

https://doi.org/10.1021/acsnano.3c13039
ACS Nano 2024, 18, 8392−8410

Figure 7. continued

< 0.05. (c) *In vivo* bioluminescence images of the mice bearing A549-FLuc lung orthotopic tumors during the study. (d–g) *Ex vivo* characterization of the collected lungs on day 41: (d) photographs, (e) bioluminescent images, (f) *ex vivo* bioluminescent quantification, and (g) weights of the collected lungs. Data are represented as mean ± standard deviation (G1, G2, G3, $n = 6$; G4, $n = 5$). Statistical analysis was performed using one-way ANOVA with Tukey's multiple comparisons test, *$p < 0.05$. (h, i) Histopathological analysis of the collected lungs. (h) Data of the H&E-stained lung tissues, and IHC-stained lung tissues against cleaved caspase-3, cleaved PARP, K_i-67, CD31, and VEGF (left to right). (i) Statistical summary of tumor mass number and percentages of cleaved caspase-3, cleaved PARP, K_i-67, CD31, and VEGF-positive cells in each group. Data are represented as mean ± standard deviation ($n = 6$). Statistical analysis was performed using one-way ANOVA with Tukey's multiple comparisons test, *ns,* not significant; **$p < 0.01$; ***$p < 0.001$; ****$p < 0.0001$ versus the G1 group. $^{\#\#}p < 0.01$; $^{\#\#\#}p < 0.001$; $^{\#\#\#\#}p < 0.0001$ versus the G2 group. $^{\&}p < 0.05$; $^{\&\&}p < 0.01$; $^{\&\&\&}p < 0.001$ versus the G3 group.

disulfide bonds prior to secretion, except for the LC which can be secreted as free chains.[45,46] Upon delivery of both mRNA transcripts to HeLa cells in a 2:1 ratio (w/w; HC:LC), Western blot analysis of the cell lysates under nonreducing conditions revealed the presence of bevacizumab with the same molecular weight as the recombinant bevacizumab protein (Figure S15). Additionally, it was demonstrated that the conditioned media contained bevacizumab protein, confirming the successful secretion of bevacizumab following mRNA transfection (Figures 6c). Under reducing conditions, breaking a disulfide bond, two bands corresponding to HC and LC proteins were detected at around 50 and 25 kDa, respectively (Figures 6c and S15). To simultaneously deliver the two mRNA transcripts, we encapsulated both in F6 NPs in a 2:1 ratio (w/w; HC:LC). The resulting F6 NPs displayed an average diameter of 179.5 ± 3.39 nm in DLS and a spherical morphology in TEM imaging (Figure S16), similar to those of F6 NPs encapsulating a reporter mRNA. Upon treating A549 cells with bevacizumab mRNA-loaded F6, the presence of bevacizumab protein was confirmed in the conditioned media (Figure 6d). It indicates the successful F6-mediated bevacizumab mRNA transfection and the subsequent secretion of the antibody. When evaluating the antibody production from F6-delivered WT and m1Ψ mRNA transcripts, WT mRNA resulted in a higher secretion of bevacizumab compared to that of m1Ψ mRNA (Figure 6e). In contrast, the systemic administration of F6 containing m1Ψ mRNA to mice led to a higher serum concentration of bevacizumab than that containing WT mRNA (Figure 6f). However, no statistical significance was observed both *in vitro* and *in vivo* (Figure 6e,f). The serum concentrations of bevacizumab reached their peaked at 24 h postadministration and gradually declined to undetectable levels by 7 days postadministration (Figure 6f). Based on these results, m1Ψ mRNA was chosen for its less immunogenic nature compared to WT mRNA, particularly with respect to the innate immune system.[47] The pharmacokinetics of a recombinant bevacizumab protein after intraperitoneal (IP) administration in mice (Figure S17) was also studied. Overall, serum concentrations of bevacizumab from F6-delivered mRNA were lower than those of the bevacizumab product (Figures 6f and S17). This probably resulted from the low mRNA dose and lung-specific transfection of F6.

To assess whether F6-mediated mRNA delivery enhances the pulmonary distribution of bevacizumab, we measured the bevacizumab concentration in the lungs and serum following the systemic administration of bevacizumab mRNA-loaded F6. These measurements were compared to those from intraperitoneal administration of recombinant bevacizumab protein. Regarding the intraperitoneally administered recombinant bevacizumab protein, concentrations exhibited a dose-dependent rise in both serum and lung lysates, ranging from 0.0125 to 5 mg/kg (Figure S18a,b). The antibody concentrations were lower in the lungs compared to the serum, and at a dose of 0.0125 mg/kg, the antibody concentrations in the lung lysates were below the lower limit of quantification. An intravenous administration of F6-complexed bevacizumab mRNA at a dose of 0.5 mg/kg resulted in antibody concentrations in the serum comparable to the intraperitoneal dose of 0.0125 mg/kg of recombinant protein (Figure S18a,b). Notably, the intravenous administration of bevacizumab mRNA at the given dose achieved higher antibody concentrations in the lung lysates compared to the intraperitoneal dose of 0.25 mg/kg of recombinant bevacizumab protein, suggesting a more pronounced pulmonary distribution of the antibody facilitated by F6-assisted lung transfection (Figure S18b). When represented in lung lysate/serum ratios, the inclination of the antibody distribution toward the lungs became conspicuous (Figure 6g). It was shown that the distribution of the antibody was more concentrated in the lungs than in the serum when administered in the form of F6-loaded mRNA. Conversely, intraperitoneal administration of the recombinant antibody resulted in a more prominent distribution to the bloodstream than to the pulmonary tissues. Despite the distinct administration routes of the two modalities and the assay being conducted at a single time point, the results appear to robustly support the potential advantages of F6-mediated mRNA delivery in enhancing the pulmonary availability of therapeutic proteins.

Next, we investigated the biocompatibility of F6 through clinical blood chemistry tests related to liver function (Figure S19). In the examined parameters, there were no concerning signs observed in the mouse serums collected at 24 h after intravenous injections of empty F6, bevacizumab mRNA-loaded F6 at a dose 0.5 mg/kg, and intraperitoneally administered recombinant bevacizumab protein, as compared to those from naïve mice. Despite slight increases in alanine aminotransferase (ALT) in the bevacizumab mRNA-loaded F6 treatment group, the results remained within their normal ranges.[48]

Having confirmed that F6-mediated mRNA delivery produced bevacizumab *in vivo*, we evaluated the antitumor effects of our approach in NSCLC orthotopic mouse models. Two orthotopic mouse tumor models, utilizing A549-FLuc cells, were used to represent different phases of progression in NSCLCs (Figure S20).[49] The model established through intravenous administration of A549 cells mimics the late stage of NSCLC, where cancer cells circulate through the bloodstream and disseminate across the lungs. Meanwhile, the transpleural A549 model aimed to replicate the progression of human NSCLC, starting from a localized intraparenchymal tumor to the subsequent formation of metastasis. Once tumor development in the lungs was confirmed by bioluminescence, the mice were treated with various regimens: PBS, empty F6 NPs, a recombinant bevacizumab protein, or F6 NPs carrying bevacizumab mRNA (Figure 7a). Treatments were adminis-

https://doi.org/10.1021/acsnano.3c13039
ACS Nano 2024, 18, 8392–8410

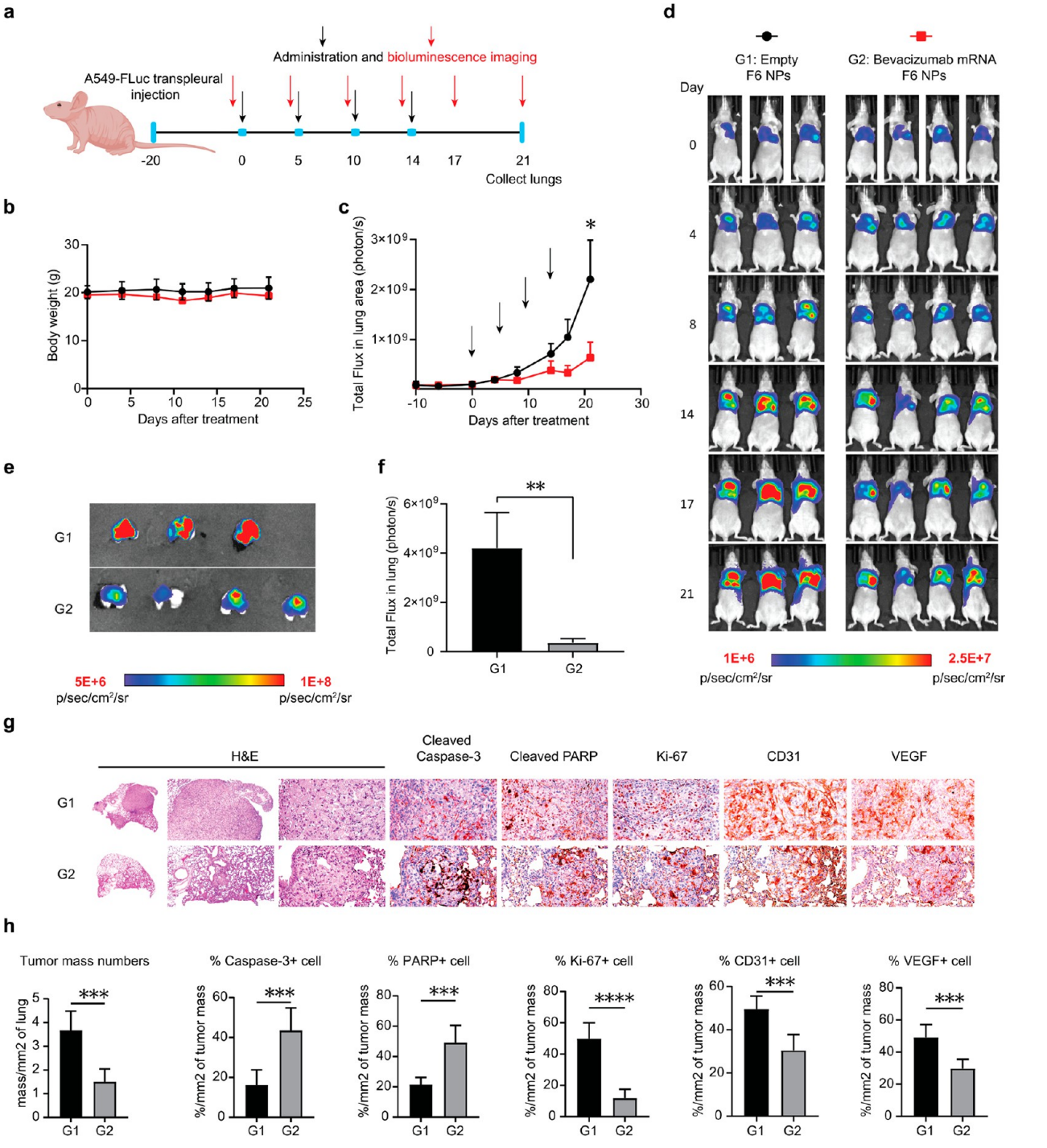

Figure 8. Antitumor activity of F6-delivered bevacizumab mRNA therapy in the orthotopic NSCLC mouse model developed by A549-FLuc transpleural injection. (a) Schematic diagram of dosing regimens (black arrows) and bioluminescence imaging schedules (red arrows) for treating A549-FLuc lung orthotopic tumors. (b) Body weight changes of mice for the study. (c, d) Monitored bioluminescence from the transpleurally induced A549-FLuc lung tumors. (c) Quantified luciferase expression in the lungs of the mice treated with empty F6 NPs (G1, black) or F6 NPs carrying bevacizumab mRNA (G2, red). Data are represented as mean ± standard deviation (G1 $n = 3$; G2 $n = 4$). Statistical analysis was performed using a two-tailed Student's *t*-test, $*p < 0.05$ at 21 days. (d) *In vivo* bioluminescence images of the mice bearing A549-FLuc orthotopic lung tumors during the study. (e, f) Ex vivo characterization of the collected lungs on day 21: (e) bioluminescence images and (f) quantified bioluminescence of the collected lungs. Data are represented as mean ± standard deviation (G1, $n = 3$; G2, $n = 4$). Statistical analysis was performed using a two-tailed Student's *t*-test, $**p < 0.01$ at 21 days. (g,h) Histopathological analysis of the collected lungs. (g) Data of the H&E-stained lung tissues, and IHC-stained lung tissues against cleaved caspase-3, cleaved PARP, K_i-67, CD31, and VEGF (left to right). (h) Statistical summary of the tumor mass and percentages of cleaved caspase-3, cleaved PARP, K_i-67, CD31, and VEGF-positive cells in each group. Data are represented as mean ± standard deviation ($n = 6$). Statistical analysis was performed using a two-tailed Student's *t*-test, $***p < 0.001$; $****p < 0.0001$.

https://doi.org/10.1021/acsnano.3c13039
ACS Nano 2024, 18, 8392−8410

tered weekly, and tumor growth was monitored by bioluminescence imaging of the cancer cells (Figure 7b). In animals treated with PBS and empty NPs (G1 and G2, respectively), the luminescent signals increased in the lungs over time, indicating rapid tumor progression (Figure 7b,c). When mice were treated with the bevacizumab product (G3), a slight suppression of bioluminescent signals was observed compared with those of the PBS- or empty NP-treated group. Notably, treatment with F6 NPs encapsulating bevacizumab mRNA resulted in significantly lower bioluminescence (G4), suggesting the therapeutic effects of F6-mediated bevacizumab mRNA against NSCLCs. At the end of day 41, the lungs of each group were harvested for in-depth evaluation of the tumor tissues (Figure 7d–g). In macroscopic analysis, the murine lungs that received PBS or empty F6 NP treatment had larger sizes and more tumor nodules with abnormally colored patches on the tissue surfaces compared with those treated with a recombinant bevacizumab protein (Avastin, Roche) or bevacizumab mRNA (Figure 7d). Moreover, when imaged for bioluminescence, it was clear that the lungs from G3 and G4 exhibited lower luciferase expression than those from G1 and G2, indicating the anticancer effects of bevacizumab (Figure 7e,f). Furthermore, the lung weight in G4 mice was significantly lower than that in G2 mice (Figure 7g). Considering that the body weights of the mice were similar in all groups (Figure S21), the lower weight of the lungs in G4 suggests selective inhibition of tumor growth in the pulmonary system (Figure 7g). The lungs were subjected to histopathological analysis to further assess the tumor-inhibitory effects of F6 NP-assisted bevacizumab mRNA therapy (Figure 7h,i). Hematoxylin and eosin (H&E)-stained tissues showed that G3 and G4 mice demonstrated considerable reduction in the areas occupied by cancer cells in the lungs compared with the other groups (Figures 7h and S22). This was corroborated by the significantly lower number of tumor masses formed in the intrapulmonary spaces (Figure 7i). Of note, G4 had significantly smaller tumor masses per area when compared to G3, suggesting the therapeutic benefits of the mRNA approach over the bevacizumab protein (Figure 7i). Immunohistochemistry (IHC) staining revealed additional changes in protein markers in the lung tissues (Figure 7h,i). Cleaved caspase-3 and cleaved poly(ADP-ribose) polymerase (PARP) are useful indicators of tumor apoptosis.[50] We found that these markers in the intrapulmonary tumor mass significantly increased in G3 and G4 compared to G1 and G2, demonstrating the therapeutic effects of bevacizumab against NSCLCs (Figure 7h,i). Importantly, G4 displayed significantly greater levels of caspase-3 and cleaved PARP than G3, supporting the therapeutic potential of F6-mediated bevacizumab mRNA therapy over that of bevacizumab protein therapy. K_i-67 is a prominent marker of cancer cell proliferation and metastasis.[51] The K_i-67 levels in the lung tissue sections were lower in G3 and G4 than in G1 and G2, indicating inhibition of tumor proliferation and growth due to bevacizumab activity (Figure 7h,i). Again, G4 produced a more significant inhibition of K_i-67 percentage scores than G3. CD31 and VEGF are well-defined markers of angiogenesis.[52] Bevacizumab treatments, both with bevacizumab protein (G3) and F6-mediated mRNA (G4), led to a reduction of CD31 and VEGF expression compared to the controls (i.e., G1 and G2) in the lungs (Figure 7h,i). In particular, the levels of CD31 and VEGF were significantly lower in G4 than those in G3, demonstrating a more significant suppression of NSCLC angiogenesis by mRNA therapy. Collectively, bevacizumab treatment effectively inhibited NSCLC progression, and, especially, F6-assisted bevacizumab mRNA delivery displayed greater antitumor efficacy against NSCLC than bevacizumab through efficient induction of apoptosis and suppression of angiogenesis.

We additionally examined the therapeutic efficacy of F6-assisted bevacizumab mRNA therapy in another orthotopic NSCLC mouse model. The A549-FLuc cells were transpleurally injected directly into the lungs through the intercostal space (Figure 8a). This orthotopic NSCLC mouse model is useful not only because it provides localized intraparenchymatous tumor,[53] but also because it mimics a pleural metastasis of lung carcinoma that typically worsens the prognosis in patients with NSCLC.[54] With this model, we continued to assess the therapeutic potential of the F6-assisted bevacizumab mRNA therapy. The body weights of the animals were not significantly different between the empty F6 NPs (G1) and F6 NPs carrying bevacizumab mRNA (G2) (Figure 8b). When bioluminescence was measured in the implanted lung cancer cells, an apparent suppression of tumor growth was observed in G2, whereas G1 showed rapid tumor growth in the pulmonary system (Figure 8c,d). In the following *ex vivo* analysis, 21 days after the initial treatment, the luminescent signals from the harvested lungs were significantly lower in the mRNA-treated lungs (G2) than in the empty NP-treated lungs (G1), indicating the antitumor efficacy of bevacizumab mRNA delivery (Figure 8e,f). We also conducted a histopathological analysis of these lungs, and H&E staining revealed potent inhibition of tumor mass numbers and mass-occupied regions by bevacizumab mRNA (Figures 8g,h, and S23). Using IHC staining, we found that mRNA treatment led to apoptosis in the tissues, as shown by significant increases in cleaved caspase-3 and PARP. In addition, the K_i-67-positive percentage was significantly smaller in G2 than in G1, indicating inhibition of tumor growth due to bevacizumab mRNA treatment. Lastly, the levels of the angiogenesis markers CD31 and VEGF showed that F6-mediated bevacizumab mRNA delivery suppressed pulmonary angiogenesis in NSCLC. Taken together, our results suggest that delivering bevacizumab mRNA to PECs using F6 NPs could be used to treat NSCLCs through intrapulmonary production of this protein and result in the efficient suppression of angiogenesis.

CONCLUSIONS

Recent advances in nanomedicine have led to the clinical use of synthetic mRNA, expanding its applications beyond immunization to include therapeutic treatments. The ability of mRNA to express intracellular, extracellular, or transmembrane proteins provides a broad spectrum of therapeutic opportunities in anticancer therapy.[55,56] Such therapeutic potential of mRNA can be augmented by target-specific nanocarriers.[18,29,57,58] LNPs, the most advanced nonviral vectors, primarily transfect hepatocytes following intravenous administration.[59] Although LNP-mediated mRNA delivery can result in antibody secretion into the circulation from transfected hepatocytes,[60,61] the large molecular weight and polarity of antibodies often limit their distribution to cancerous tissues.

In this study, we explored the therapeutic potential of bevacizumab-encoded synthetic mRNA delivered by using PEC-targeting PBAE NPs. We hypothesized that preferential mRNA delivery to PECs achieved by PBAE NPs could enhance the pulmonary availability of bevacizumab and, therefore, inhibit NSCLC tumor growth. The antiangiogenic effects of bevacizumab are based on the blockade of VEGF. VEGF receptors associated with NSCLCs are primarily expressed in

https://doi.org/10.1021/acsnano.3c13039
ACS Nano 2024, 18, 8392–8410

the PECs. Therefore, it was conceivable that *in situ* production of bevacizumab by mRNA delivered to PECs would block VEGF more efficiently. To target PECs more efficiently, a library of PBAE polymers and selected PBAE-D were screened based on their endosomal escape behaviors and mRNA transfection efficiencies. The formulation study revealed that the transfection site and delivery efficiency *in vivo* were influenced not only by the contents of the cationic polymers but also by the tail length of PEG lipids and the PEG molarity in PBAE NPs. We subsequently aimed to elucidate the mechanism behind organ-selectivity of two NPs, F1 and F6, by examining their interactions with blood proteins and analyzing how their particle sizes changed upon contact with plasma. These two NPs displayed distinct properties in both the size and composition of their protein coronas, influencing their *in vitro* mRNA transfection efficiency. These distinctions may carry implications for their *in vivo* behaviors and subsequent mRNA delivery. Nevertheless, the precise mechanism accountable for the targeted delivery of mRNA to the lungs and spleen by PBAE NPs is yet to be determined, and it awaits further investigation in the future. By leveraging the lung-targeting behaviors of F6, we aimed to deliver the therapeutic antibody bevacizumab in the form of mRNA to PECs for the treatment of NSCLC. The synthesized mRNA molecules encoding HC or LC of bevacizumab resulted in the production and secretion of the antibody upon their cellular delivery, and the encapsulation of bevacizumab mRNA within F6 NPs led to the production of pulmonary and circulating bevacizumab antibodies following intravenous administration. In orthotopic mouse models of NSCLC, bevacizumab treatments, both F6-mediated mRNA therapy and recombinant protein, were effective in suppressing tumor growth. Notably, F6-delivered bevacizumab mRNA therapy significantly inhibited tumor cell proliferation. Furthermore, the histopathological analysis of the mRNA-treated lungs revealed more significant inhibition of angiogenesis and metastasis and enhanced induction of apoptosis than the bevacizumab protein treatment.

In summary, this study provides evidence for the principle of delivering bevacizumab mRNA for the treatment of NSCLCs. Using PBAE-based NPs, PEC-selective bevacizumab mRNA delivery and the blockade of VEGF in pulmonary tissues were achieved, which could be advantageous for eradicating angiogenesis in NSCLCs. We acknowledge several limitations of this study, such as a discrepancy between NP biodistribution and transfection sites after mRNA administration as well as partial validation of organ-selective mechanisms of the NPs. Despite these limitations, our study highlighted the potential use of synthetic mRNA to produce therapeutic antibodies for cancer treatment.

MATERIALS AND METHODS

Materials. Bisphenol A glycerolate (1 glycerol/phenol) diacrylate, 1-(2-aminoethyl)pyrrolidine, and 2-(2-aminoethyl)-1-methylpyrrolidine were purchased from Sigma-Aldrich. Dodecylamine, 1,3-diaminopropane, and 4-amino-1-butanol were purchased from Tokyo Chemical Industry (TCI). 1,2-Dioleoyl-*sn*-glycero-3-phosphoethanolamine (DOPE) and 1,2-distearoyl-*sn*-glycero-3-phosphoethanolamine-*N*-[methoxy (polyethylene glycol)-2000] (ammonium salt) (DSPE-PEG_{2K}) were purchased from Avanti Polar Lipids. 1,2-Dimyristoyl-*rac*-glycero-3-methoxypolyethylene glycol-2000 (DMG-PEG_{2K}) was purchased from Nanosoft Polymers. Urea, thiourea, 3-((3-cholamidopropyl) dimethylammonio)-1-propanesulfonate (CHAPS), dithiothreitol (DTT), Tris base, Bradford solution, acrylamide, iodoacetamide, bis-acrylamide, SDS, acetonitrile, trifluoroacetic acid, α-cyano-4-hydroxycinnamic acid, 4-sulfophenyl isothiocyanate, hydroxycinnamic acid, sodium bicarbonate, and ammonium bicarbonate were purchased from Sigma-Aldrich (St. Louis, MO, U.S.A.). Pharmalyte (pH 3.5−10) was obtained from Amersham Biosciences, and IPG DryStrips (pH4−10NL, 24 cm) were purchased from Genomine Inc. Modified porcine trypsin (sequencing grade) was obtained from Promega (Madison, WI, U.S.A.). The CleanCap FLuc mRNA was purchased from TriLink BioTechnologies. PB-GFP-Gal8 was a gift from Jordan Green (#127191, Addgene), and pCAG-luciferase was a gift from Snorri Thorgeirsson (#55764, Addgene). PiggyBac transposase vector was purchased from System Biosciences (PB210PA-1). D-Luciferin potassium salt was purchased from Biosynth. A HiScribe T7 mRNA Kit with CleanCap Reagent AG, *E. coli* poly(A) polymerase, and Monarch RNA Cleanup Kit were purchased from New England Biolabs (NEB, Ipswich, MA, U.S.A.).

Synthesis of PBAE Polymers. Monomer solutions were prepared by using *N*,*N*-dimethylformamide. Bisphenol A glycerolate diacrylate (888.0 mg), 4-amino-1-butanol (68 mg), 1-(2-aminoethyl)pyrrolidine (87.4 mg), or 2-(2-aminoethyl)-1-methylpyrrolidine (99.2 mg), and dodecylamine (143 mg) were added to a 20 mL glass vial. The mixture was heated at 90 °C for 48 h for Michael addition reaction to proceed and then cooled to room temperature. The polymers were end-capped by adding 240 mg of 1,3-diaminopropane. The end-capping reactions were stopped after 24 h. The product mixtures were diluted in diethyl ether (product:diethyl ether = 1:4, v/v) and vigorously vortexed. The mixtures were centrifuged at 1250 RCF. The supernatants were removed, and the solid polymers were collected. After additional washing with diethyl ether, the polymers were completely dried under reduced pressure. The synthesized polymers were confirmed by ^{1}H NMR and stored at −20 °C.[17,18,62]

Preparation and Characterization of mRNA-Loaded PBAE Nanoparticles. mRNA was diluted in 25 mM sodium acetate buffer (pH 5.0) as the aqueous phase. Mixtures of PBAE, DOPE, and PEG lipids (DMG-PEG_{2K} or DSPE-PEG_{2K}) were dissolved in ethanol. NPs were formulated by vigorously mixing the two phases. For *in vitro* and *in vivo* assays at a dose of 0.1 mg of mRNA/kg, the ratio of the aqueous phase to the ethanol phase was 1:1 (v/v). For *in vivo* studies, at a dose of 0.5 mg of mRNA/kg, the ratio was 3:1 (v/v). The assembled NPs were dialyzed against PBS at 4 °C for 2 h using a dialysis tubing (12000 Da, molecular-weight cutoff).[18] The hydrodynamic diameter and PDI of NPs were assessed through dynamic light scattering using a Zetasizer Nano S90 (Malvern, U.K.). The zeta potential of NPs was measured with a Zetasizer Nano ZEN 2600 (Malvern, U.K.). NP morphology was characterized using TEM (Hitachi H-7600) on carbon-coated copper grids.[63] mRNA encapsulation was calculated using the RiboGreen Assay kit (Thermo Fisher Scientific), as described previously.[18] The apparent pK_a values of mRNA-loaded PBAE NPs were determined by using TNS assays by measuring surface ionization. Briefly, buffers from pH 2.0 to 12.0 in increments of 0.5 were prepared by adjusting an aqueous solution (20 mM sodium phosphate, 25 mM citrate, 20 mM ammonium acetate, and 150 mM NaCl) with 0.1 N NaOH and 0.1 N HCl. Aliquots (100 μL) of the buffers were added to a 96-well black microplate. Then, TNS solution in the final concentration of 6 μM and PBAE NPs in 3.5 μg of polymer were added to each well. Fluorescence intensity was measured using a multimode microplate reader (Tecan Trading AG, Switzerland) at excitation and emission wavelengths of 360 and 465 nm, respectively. The measured fluorescence was normalized to the minimum fluorescence value, and curve fitting was applied to the normalized fluorescence data. The apparent pK_a of each PBAE NP was determined as the pH value corresponding to half of the maximum fluorescence level.[57]

Cell Culture. Human cancer cell lines HeLa, Hep G2, and A549 were purchased from the Korea Cell Line Bank. HUVEC was obtained as a gift from Professor Jae-Ryong Kim (Yeungnam University Medical Center). HeLa, Hep G2, and A549 cells were cultured in complete DMEM (cDMEM) containing 10% FBS and 1% penicillin/streptomycin at 37 °C in an incubator with 5% CO_2. HUVECs were cultured in endothelial cell growth medium (CC-3162 EGM-2 BulletKit, Lonza).

https://doi.org/10.1021/acsnano.3c13039
ACS Nano 2024, 18, 8392−8410

***In Vitro* Cell Viability Assay.** The cytotoxicity of PBAE NPs was tested by using MTS assays. Briefly, cells were seeded in 96-well plates at a density of 1×10^4 cells/well and incubated for 24 h. The cells were then treated with mRNA-loaded PBAE NPs. After 5 h, 20 μL of MTS solution was added, followed by 1 h of incubation at 37 °C and 5% CO_2. The absorbance was measured at 490 nm (A) using a microplate reader. Cell viability was calculated using the following equation: Cell viability (%) = $(A_{sample} - A_{blank})/(A_{control} - A_{blank}) \times 100$.

Cellular Uptake Study. The cellular uptake of mRNA into HeLa cells was evaluated by using flow cytometry (BD FACSCalibur, BD Biosciences). HeLa cells were seeded into a 12-well plate at 10^5 cells/well for 24 h. Cells were exposed to various treatments at a Cy5-labeled mRNA concentration of 200 ng/well for 4 h. After washing with PBS, the cells were harvested and analyzed by flow cytometry, with PBS-treated cells as the control.[63]

Preparation of HeLa-Gal8-GFP Cells and Gal8 Recruitment Study. HeLa cells were seeded in a 6-well plate at a density of 2×10^5 cells/well. The cells were treated with 0.5 μg of PB-GFP-Gal8 and 0.2 μg of PiggyBac transposase vector/well using PBAE-D NPs as described above. After 72 h, cells were collected for positive integration by using flow cytometry. A single positive clone of HeLa-Gal8-GFP cells was prepared by limited dilution and expanded by subculture.[19,20] For the Gal8 recruitment assays, HeLa-Gal8-GFP cells were seeded on coverslips in 12-well plates at a density of 1×10^5 cells/well. After 24 h, the cells were treated with PBS, naked Cy5 mRNA, or Cy5 mRNA PBAE NPs at 200 ng of mRNA/well and incubated for 12 h. After washing with PBS, the cells were fixed with 4% paraformaldehyde, washed three times with PBS, and stained with Hoechst solution (1 μg/mL) for 5 min. Finally, the cells were mounted on slides, and image were captured using a confocal laser scanning microscope (Nikon A1+, Nikon).[19,20]

***In Vitro* Transfection Assay.** HeLa, A549, and Hep G2 cells were seeded into 96-well white plates at various densities (HeLa and A549: 20000 cells/well; Hep G2: 30000 cells/well). After 24 h, the medium was replaced with cDMEM or serum-free DMEM, and PBAE NPs were added at a dose of 25 ng of FLuc mRNA/well. After 5 h of NP treatment, the medium was replaced with fresh cDMEM and incubated for an additional 12 h. Finally, the cells were treated with 10 μL of D-luciferin solution (4 mg/mL) and incubated for 10 min at 37 °C. FLuc expression was measured using a multimode microplate reader. To characterize bevacizumab mRNA transfection, cells were seeded on a 12 well plate at 3×10^5 cells per well. After 24 h, the cells were treated with NPs carrying bevacizumab mRNA (w/w; HC:LC = 2:1) for 24 h. Subsequently, the culture media and the transfected cells were collected for Western blot. In addition, HeLa cells were seeded on a 96-well plate at 2×10^4 cells per well. After 24 h, the cells were treated with NPs at a dose of 125 ng bevacizumab mRNA/well for 24 h, followed by the collection of the culture media. Subsequently, bevacizumab concentrations in the culture media were measured using ELISA (ab237642, Abcam) according to the manufacturer's instructions.

Western Blot. Total proteins from the transfected cells were extracted using a radioimmunoprecipitation assay (RIPA) buffer containing protease inhibitors. Protein concentrations in cell-free media and cell lysates were measured by using a BCA protein assay kit (Thermo Fisher Scientific). 15 μg of total proteins was mixed with sodium dodecyl sulfate (SDS) sample buffer under nonreducing or reducing condition (denatured at 90 °C for 10 min with 5% 2-mercaptoethanol), separated on 4−10% SDS polyacrylamide gel, and transferred to PVDF membrane (Merck Millipore). The membrane was blocked using 3% BSA in Tris-Buffered Solution supplemented with 0.1% Tween-20 (TBST) for 1 h. Subsequently, it was incubated with a polyclonal goat antihuman-IgG (H+L) HRP (Jackson ImmunoResearch, 109−035−088) at 1:1,000 in the blocking buffer for 1 h at room temperature, followed by several washings with TBST. For chemiluminescence imaging, the membrane was incubated in SuperSignal West Pico Chemiluminescent Subtrate or SuperSignal West Femto Chemiluminescent Subtrate (Thermo Fisher Scientific) according to the manufacturer's instructions. For β-actin detection in cell lysates, the membrane was incubated with a mouse monoclonal anti-β-actin (Thermo Fisher Scientific, MA5−15739) at 1:10000 in the blocking buffer, followed by the secondary incubation with antimouse IgG (H+L) HRP (Promega, W4021).

Preparation of A549-FLuc Cells. A549 cells were seeded into 6-well plates and incubated for 12 h before transfection. Cells were transfected with pCAG-luciferase at 1 μg/well using Lipofectamine 3000 (Thermo Fisher Scientific) according to the manufacturer's protocol. At 24 h post-transfection, the medium was replaced with DMEM. At 48 h post-transfection, G418 sulfate (Thermo Fisher Scientific) was added to the cells according to the manufacturer's protocol. The medium was replenished twice per week, and the concentration of G418 sulfate was maintained. After 10 days, the G418-selected cells were expanded and single clones were prepared by limited dilution and expansion. A portion of the selected cells was further cultured to confirm luciferase expression at various time points. The concentration of G418 sulfate was maintained throughout the subculture.[64]

Animals. All animal experiments were performed at Yeungnam University and followed protocols approved by the Institutional Animal Care and Use Committee (IACUC) at Yeungnam University (Protocol#: 2022−023). BALB/c (5-week-old females) and BALB/c nude (5-week-old females) mice were provided by Orient Bio, Inc. (Seongnam, South Korea).

***In Vivo* Evaluation of FLuc mRNA PBAE NPs.** The formulated PBAE NPs were injected intravenously into the mice via the tail vein at a dose of FLuc mRNA of 0.1 or 0.5 mg/kg. Six hours after administration, the D-luciferin substrate (150 mg/kg) was injected intraperitoneally and incubated for 15 min. Bioluminescence imaging of the whole body and major organs was performed using the In Vivo Imaging System (IVIS; IVIS Lumina, PerkinElmer).[18,57]

***In Vivo* Biodistribution of PBAEs NPs.** The PBAE NPs loaded with Cy5-labeled mRNA were intravenously injected into BALB/c mice via the tail vein at an mRNA dose of 0.5 mg/kg. Four hours after administration, the mice were sacrificed and Cy5 fluorescence in the organs was examined using an IVIS (IVIS Lumina, PerkinElmer). The collected lungs were then processed into single-cell suspensions. Lung cells were stained with a viable dye (Zombie Green, BioLegend) according to the manufacturer's protocol. Fc block (antimouse CD16/32 antibody, BioLegend, 1:100) was used for blocking nonspecific binding, and the PEC were stained with anti-CD31-APC/Fire 750 antibody (BioLegend, 1:50). Finally, after several washes with PBS, the cells were analyzed by flow cytometry (FACSVerse, BD Biosciences).

Isolation of Proteins Adsorbed to NPs. Collection of blood proteins forming the coronas on NP surface was conducted as previously described.[30] Briefly, mouse plasma was collected from BALB/c mice, and protein aggregates were removed by centrifugation. PBAE NPs containing mRNA were incubated with mouse plasma in a 1:1 ratio (v/v) for 1 h at 37 °C under shaking. Then, NP/protein complexes were isolated by centrifugation at 16000 g for 1 h at 4 °C. Nonbound proteins were removed by washing the complexes three times with cold PBS. Throughout the processes, low-protein-binding microcentrifuge tubes were used (Thermo Fisher Scientific).

Characterization of Proteins Adsorbed to NPs by SDS-PAGE and Protein Identification via Mass Spectrometry. The isolated NP/protein pellets were resuspended in 2% SDS, and the protein concentration was measured using a bicinchoninic acid (BCA) assay. Proteins were extracted by a trichloroacetic acid (TCA)/acetone precipitation method. Extracted proteins were resuspended in the sample buffer and denatured at 90 °C for 5 min with 2-mercaptoethanol. For one-dimensional SDS-PAGE, the samples were separated on a 4−10% SDS PAGE gel, followed by staining with Imperial Protein Stain (Thermo Fisher Scientific) according to the manufacturer's protocol. Further analysis of the proteins was conducted by Genomine Inc. (Pohang, South Korea). Briefly, the NP/protein pellets isolated from the surface of PBAE NPs were resuspended in the lysis solution consisting of 8.4 M urea, 2 M thiourea, 4% (w/v) CHAPS, 1% (w/v) DTT, 2% (v/v) Pharmalyte, and 40 mM, followed by 1 h vortexing to extract proteins. The protein extracts were subjected to centrifugation at 12,000 rpm at 25 °C. Protein concentration in the supernatant was determined by Bradford assay. Immobilized pH gradient dry strips (4−10 NL IPG, 24 cm, Genomine, South Korea)

https://doi.org/10.1021/acsnano.3c13039
ACS Nano 2024, 18, 8392−8410

were equilibrated for 12−16 h with the buffer containing 7 M urea, 2 M thiourea, 2% CHAPS, 1% DTT, and 1% Pharmalyte, and 120 μg of protein sample was loaded per strip. Isoelectric focusing was performed at 25 °C using a Multiphor II electrophoresis unit and EPS 3500 XL power supply (Amersham Biosciences) following the manufacturer's instruction. Before the second dimensional separation, strips were incubated in the equilibrium buffer twice, each time for 10 min. Equilibrated strips were inserted onto SDS-PAGE gels (20 × 24 cm, 10−16%). SDS-PAGE was performed using Hoefer DALT 2D system (Amersham Biosciences) following the manufacturer's instruction. Then, the gels underwent alkaline silver staining. Quantitative analysis of digitized images was conducted using PDQuest software (version 7.0, BioRad) following the manufacturer's protocol. The quantity of each spot was normalized to the total valid spot intensity. Protein spots that exhibited a significant expression variation, deviating over 2-fold in their expression level compared to a control, were selected. For protein identification by peptide mass fingerprinting (PMF), protein spots were excised, digested with trypsin (Promega), mixed with α-cyano-4-hydroxycinnamic acid in 50% acetonitrile/0.1% TFA, and subjected to matrix-assisted laser desorption/ionization-time-of-flight mass spectrometry (MALDI-TOF) analysis (Autoflex Speed LRF, Bruker). Spectra were collected from 300 shots per spectrum over m/z range 700−4000 and calibrated by two-point internal calibration using trypsin autodigestion peaks (m/z 842.5099, 2211.1046). The peak list was generated using the flexAnalysis software (version 3.4, Bruker), with the following threshold values: 500 for the minimum resolution of monoisotopic mass, 5 for S/N. For protein identification by PMF, the search program MASCOT, developed by Matrix Science (http://www.matrixscience.com/), was employed. The parameters for the database search included trypsin as the cleaving enzyme, a maximum of one missed cleavage, iodoacetamide (Cys) as a complete modification, oxidation (Met) as a partial modification, monoisotopic masses, and a mass tolerance of ±0.2 Da. PMF acceptance criteria were based on probability scoring.

***In Vitro* Transcription of Bevacizumab mRNA.** The codon-optimized sequences of the heavy and light chains of bevacizumab were synthesized and cloned into pBHA plasmids by Bioneer (Daejeon, South Korea). The plasmids were linearized using BspQI (NEB) and precipitated using phenol:chloroform:isoamyl alcohol extraction. *In vitro* transcription was performed using a HiScribe T7 mRNA Kit at 37 °C for 2 h, and 5′ capping was conducted cotranscriptionally using CleanCap Reagent AG (NEB) according to the manufacturer's protocol. The synthesized mRNA was purified by LiCl precipitation. Subsequently, polyadenylation and purification were performed using a Poly(A) Polymerase Kit (NEB) and Monarch RNA Cleanup Kit (NEB) according to the manufacturer's protocols, respectively.[59] Chemically modified mRNA was synthesized by completely replacing UTP with N1-methylpseudouridine-5′-triphosphate. For Cy5-labeled mRNA synthesis, UTP was partially replaced with Cy5-UTP (Cy5-UTP:UTP = 1:2 molar ratio). The integrity of the synthesized mRNA was assessed by denaturing agarose gel electrophoresis and visualized with ethidium bromide staining.

***In Vivo* Evaluation of PBAE-Delivered Bevacizumab mRNA Transfection.** PBAE NPs encapsulating bevacizumab mRNA were intravenously injected into the tail vein of female BALB/c mice (5−6 weeks old). The positive control, a recombinant bevacizumab protein (Avastin, Roche), was injected intraperitoneally. For pharmacokinetic studies, mouse blood samples were collected by submandibular bleeding or cardiac puncture and processed for serum extraction by centrifugation at 2000 RCF for 20 min at 4 °C.[65] For clinical chemistry studies, mouse plasma was collected and analyzed at the Kyungpook national university animal hospital (Daegu, South Korea), with naïve mice as the negative control. To estimate the pulmonary distribution of bevacizumab 24 h after administering bevacizumab mRNA or recombinant protein, mouse serum and lung lysates were collected. Blood was collected from euthanized mice via the hepatic portal vein, and the lungs were harvested after perfusion with 20 mL sterile PBS through the right ventricle until they turned white. Total proteins from the lungs were extracted in RIPA buffer containing protease inhibitors by using a tissue grinder. Concentration of bevacizumab was determined using ELISA as described previously.

Development and Treatment of Orthotopic NSCLC Mouse Models. The orthotopic A549-FLuc IV injection model was established as described previously.[66,67] Briefly, 1 × 10^6 A549-FLuc cells in PBS were directly injected into the tail vein. After 7 days, bioluminescence images were monitored weekly to measure tumor growth. Mice were divided into four groups after 2 weeks and intravenously administered PBS, empty F6 NPs, and bevacizumab mRNA F6 NPs at 0.5 mg/kg; or intraperitoneally injected with bevacizumab 5 mg/kg. At the end of the experiment, all mice were euthanized and their lungs were harvested, photographed, and fixed using 10% formalin. The orthotopic model by A549-FLuc transpleural injection was established, as described previously.[53] For each mouse, 3 × 10^6 A549-FLuc was prepared in 20 μL of a solution containing 50% of the mouse sarcoma extracellular matrix (Matrigel, Corning Life Sciences) in DMEM that was injected directly into the lungs to a depth of 4 mm through the pleura. Bioluminescence images were monitored weekly, and the mice were divided into two groups after 3 weeks of treatment with empty F6 NPs or bevacizumab mRNA F6 NPs. Tumor growth was measured twice a week using bioluminescent imaging as described above. All mice were euthanized immediately after the final *in vivo* bioluminescence imaging. The lungs were harvested as previously described.

Histological and Immunohistochemical Analyses. Equal regions of the individual left lung lobes were cross-trimmed. All crossly trimmed lung parts were refixed in 10% neutral buffered formalin for 24 h, and six serial 3−4 μm sections were prepared in each paraffin block. Representative sections were stained with hematoxylin and eosin for general histopathological profiles or with avidin−biotin-peroxidase complex (ABC)-based immunohistochemistry for cleaved caspase-3, PARP, K_i-67, CD31, and VEGF. One or two histological fields in each orthotopic lung-left-lobe tissue, for a total of six lung histological fields focused on the formed tumor masses, were considered for statistical analysis and histopathological inspection.

Statistical Analysis. Data are shown as the mean ± standard deviation. Statistical analyses were performed using Prism 8 software (GraphPad, CA, U.S.A.). Statistical tests are provided in the figure legends.

ASSOCIATED CONTENT

Supporting Information

The Supporting Information is available free of charge at https://pubs.acs.org/doi/10.1021/acsnano.3c13039.

Supporting table and figures: ^{1}H NMR data of synthesized PBAEs and bisphenol A glycerolate (1 glycerol/phenol) diacrylate; *In vitro* characterization of PBAE NPs in HUVECs; Representative confocal images of HeLa-Gal8-GFP cells; *Ex vivo* bioluminescence of organs; Schematic illustration of the protein corona formation; Gating strategy for flow cytometric analysis; Template bevacizumab DNA sequences; Western blot analysis; Bevacizumab concentrations in mouse serum and lung lysates; Clinical blood chemistry test; *In vitro* bioluminescence of the A549-FLuc cells; Body weight; Tumor mass-occupied regions; Compositions of PBAE-D nanoparticles (PDF)

AUTHOR INFORMATION

Corresponding Authors

Jeonghwan Kim − *College of Pharmacy, Yeungnam University, Gyeongsan 38541, Republic of Korea;* orcid.org/0000-0002-1697-5107; Email: jeonghwankim@yu.ac.kr

Jong Oh Kim − *College of Pharmacy, Yeungnam University, Gyeongsan 38541, Republic of Korea;* orcid.org/0000-0002-4929-851X; Email: jongohkim@yu.ac.kr

https://doi.org/10.1021/acsnano.3c13039
ACS Nano 2024, 18, 8392−8410

Authors

Ngoc Duy Le − *College of Pharmacy, Yeungnam University, Gyeongsan 38541, Republic of Korea*

Bao Loc Nguyen − *College of Pharmacy, Yeungnam University, Gyeongsan 38541, Republic of Korea*

Basavaraj Rudragouda Patil − *College of Pharmacy, Yeungnam University, Gyeongsan 38541, Republic of Korea*

HeeSang Chun − *College of Pharmacy, Yeungnam University, Gyeongsan 38541, Republic of Korea*

SiYoon Kim − *College of Pharmacy, Yeungnam University, Gyeongsan 38541, Republic of Korea*

Thi Oanh Oanh Nguyen − *College of Pharmacy, Yeungnam University, Gyeongsan 38541, Republic of Korea*

Sunil Mishra − *College of Pharmacy, Yeungnam University, Gyeongsan 38541, Republic of Korea;* orcid.org/0000-0001-8152-0742

Sudarshan Tandukar − *College of Pharmacy, Yeungnam University, Gyeongsan 38541, Republic of Korea*

Jae-Hoon Chang − *College of Pharmacy, Yeungnam University, Gyeongsan 38541, Republic of Korea*

Dong Young Kim − *College of Pharmacy, Yeungnam University, Gyeongsan 38541, Republic of Korea*

Sung Giu Jin − *Department of Pharmaceutical Engineering, Dankook University, Cheonan 31116, Republic of Korea;* orcid.org/0000-0003-1558-5155

Han-Gon Choi − *College of Pharmacy, Hanyang University, Ansan 15588, Republic of Korea*

Sae Kwang Ku − *College of Korean Medicine, Daegu Haany University, Gyeongsan 38610, Republic of Korea*

Complete contact information is available at: https://pubs.acs.org/10.1021/acsnano.3c13039

Author Contributions

N.D.L., J.K., and J.O.K. are responsible for the study, experimental design, and data analyses. H.C., S.K., N.D.L., and J.K. designed and synthesized mRNA. B.R.P. and N.D.L. synthesized the polymers. B.L.N., T.O.O.N., S.T., N.D.L., and D.Y.K. generated HeLa-Gal8-GFP and A549-FLuc cells. S.M. and J.-H.C. analyzed the samples using flow cytometry. B.L.N., T.O.O.N., N.D.L. conducted Western blot experiments. S.K.K. conducted histological and immunohistochemical analyses. S.G.J. and H.-G.C. helped to plan and interpret *in vivo* experiment. The manuscript was written by N.D.L., J.K., and J.O.K., with contributions from all the authors.

Notes

The authors declare no competing financial interest.

ACKNOWLEDGMENTS

This work was supported by the National Research Foundation (NRF) of Korea Grant funded by the Korean Government (NRF 2021R1A2C3009556, 2022R1A5A2018865). The authors thank the Core Research Support Center for Natural Products and Medical Materials (CRCNM, Yeungnam University) for technical support regarding the nanoindentation test. The schematic diagrams were created using BioRender.com.

ABBREVIATIONS

2D, two-dimensional; ALT, alanine aminotransferase; ApoB-100, apolipoprotein B-100; DMG-PEG$_{2K}$, 1,2-dimyristoyl-*rac*-glycero-3-methoxypolyethylene glycol-2000; DSPE-PEG$_{2K}$, 1,2-distearoyl-*sn*-glycero-3-phosphoethanolamine-*N*-[methoxy (polyethylene glycol)-2000] (ammonium salt); DOPE, dioleoylphosphatidylethanolamine; FBS, fetal bovine serum; Gal8, galectin 8; FLuc, firefly luciferase; GFP, green fluorescent protein; HC, heavy chain; H&E, hematoxylin and eosin; HUVEC, human umbilical vein endothelial cells; IP, intraperitoneal; IV, intravenous; LC, light chain; LNP, lipid nanoparticle; m1Ψ, N1-methylpseudouridine; NP, nanoparticle; NSCLC, nonsmall cell lung cancers; PARP, poly(ADP-ribose) polymerase; PBS, phosphate buffered saline; PBAE, poly(*β*-amino esters); PDI, polydispersity indexes; PEC, pulmonary endothelial cells; PEG, polyethylene glycol; pI, isoelectric point; TEM, transmission electron microscopy; TNS, 2-(*p*-toluidino)-6-naphthalene sulfonic acid; VEGF, vascular endothelial growth factor; WT, wild-type

REFERENCES

(1) Jiang, X.; Wang, J.; Deng, X.; Xiong, F.; Zhang, S.; Gong, Z.; Li, X.; Cao, K.; Deng, H.; He, Y.; Liao, Q.; Xiang, B.; Zhou, M.; Guo, C.; Zeng, Z.; Li, G.; Li, X.; Xiong, W. The Role of Microenvironment in Tumor Angiogenesis. *J. Exp. Clin. Cancer Res.* **2020**, *39* (1), 19.

(2) Weis, S. M.; Cheresh, D. A. Tumor Angiogenesis: Molecular Pathways and Therapeutic Targets. *Nat. Med.* **2011**, *17*, 1359−1370.

(3) Apte, R. S.; Chen, D. S.; Ferrara, N. VEGF in Signaling and Disease: Beyond Discovery and Development. *Cell* **2019**, *176*, 1248−1264.

(4) Garcia, J.; Hurwitz, H. I.; Sandler, A. B.; Miles, D.; Coleman, R. L.; Deurloo, R.; Chinot, O. L. Bevacizumab (Avastin®) in Cancer Treatment: A Review of 15 Years of Clinical Experience and Future Outlook. *Cancer Treat. Rev.* **2020**, *86*, No. 102017.

(5) Ovacik, M.; Lin, K. Tutorial on Monoclonal Antibody Pharmacokinetics and Its Considerations in Early Development. *Clin. Transl. Sci.* **2018**, *11*, 540−552.

(6) Bensch, F.; Smeenk, M. M.; van Es, S. C.; de Jong, J. R.; Schröder, C. P.; Oosting, S. F.; Lub-de Hooge, M. N.; Menke-van der Houven van Oordt, C. W.; Brouwers, A. H.; Boellaard, R.; de Vries, E. G. E. Comparative Biodistribution Analysis across Four Different 89Zr-Monoclonal Antibody Tracers-The First Step towards an Imaging Warehouse. *Theranostics* **2018**, *8*, 4295−4304.

(7) Kamba, T.; McDonald, D. M. Mechanisms of Adverse Effects of Anti-VEGF Therapy for Cancer. *Br. J. Cancer* **2007**, *96*, 1788−1795.

(8) Kim, J.; Eygeris, Y.; Gupta, M.; Sahay, G. Self-Assembled mRNA Vaccines. *Adv. Drug Delivery Rev.* **2021**, *170*, 83−112.

(9) Karmacharya, P.; Patil, B. R.; Kim, J. O. Recent Advancements in Lipid−mRNA Nanoparticles as a Treatment Option for Cancer Immunotherapy. *J. Pharm. Investig.* **2022**, *52*, 415−426.

(10) Oberli, M. A.; Reichmuth, A. M.; Dorkin, J. R.; Mitchell, M. J.; Fenton, O. S.; Jaklenec, A.; Anderson, D. G.; Langer, R.; Blankschtein, D. Lipid Nanoparticle Assisted mRNA Delivery for Potent Cancer Immunotherapy. *Nano Lett.* **2017**, *17*, 1326−1335.

(11) Yan, J.; Zhang, Y.; Du, S.; Hou, X.; Li, W.; Zeng, C.; Zhang, C.; Cheng, J.; Deng, B.; McComb, D. W.; Zhao, W.; Xue, Y.; Kang, D. D.; Cheng, X.; Dong, Y. Nanomaterials-Mediated Co-Stimulation of Toll-Like Receptors and CD40 for Antitumor Immunity. *Adv. Mater.* **2022**, *34*, No. 2207486.

(12) Li, W.; Zhang, X.; Zhang, C.; Yan, J.; Hou, X.; Du, S.; Zeng, C.; Zhao, W.; Deng, B.; McComb, D. W.; Zhang, Y.; Kang, D. D.; Li, J.; Carson, W. E.; Dong, Y. Biomimetic Nanoparticles Deliver mRNAs Encoding Costimulatory Receptors and Enhance T Cell Mediated Cancer Immunotherapy. *Nat. Commun.* **2021**, *12*, 7264.

(13) Li, Y.; Su, Z.; Zhao, W.; Zhang, X.; Momin, N.; Zhang, C.; Wittrup, K. D.; Dong, Y.; Irvine, D. J.; Weiss, R. Multifunctional Oncolytic Nanoparticles Deliver Self-Replicating IL-12 RNA to Eliminate Established Tumors and Prime Systemic Immunity. *Nat. Cancer* **2020**, *1*, 882−893.

(14) Van Hoecke, L.; Roose, K. How mRNA Therapeutics Are Entering the Monoclonal Antibody Field. *J. Transl. Med.* **2019**, *17*, 54.

(15) Bremnes, R. M.; Camps, C.; Sirera, R. Angiogenesis in Non-Small Cell Lung Cancer: The Prognostic Impact of Neoangiogenesis and the Cytokines VEGF and BFGF in Tumours and Blood. *Lung Cancer* **2006**, *51*, 143−158.
(16) Karlsson, J.; Rhodes, K. R.; Green, J. J.; Tzeng, S. Y. Poly(Beta-Amino Ester)s as Gene Delivery Vehicles: Challenges and Opportunities. *Expert Opin. Drug Delivery* **2020**, *17*, 1395−1410.
(17) Kaczmarek, J. C.; Patel, A. K.; Kauffman, K. J.; Fenton, O. S.; Webber, M. J.; Heartlein, M. W.; DeRosa, F.; Anderson, D. G. Polymer−Lipid Nanoparticles for Systemic Delivery of mRNA to the Lungs. *Angew. Chem., Int. Ed.* **2016**, *55*, 13808−13812.
(18) Kaczmarek, J. C.; Kauffman, K. J.; Fenton, O. S.; Sadtler, K.; Patel, A. K.; Heartlein, M. W.; Derosa, F.; Anderson, D. G. Optimization of a Degradable Polymer-Lipid Nanoparticle for Potent Systemic Delivery of mRNA to the Lung Endothelium and Immune Cells. *Nano Lett.* **2018**, *18*, 6449−6454.
(19) Rui, Y.; Wilson, D. R.; Choi, J.; Varanasi, M.; Sanders, K.; Karlsson, J.; Lim, M.; Green, J. J. Carboxylated Branched Poly(β-Amino Ester) Nanoparticles Enable Robust Cytosolic Protein Delivery and CRISPR-Cas9 Gene Editing. *Sci. Adv.* **2019**, *5*, No. eaay3255.
(20) Herrera, M.; Kim, J.; Eygeris, Y.; Jozic, A.; Sahay, G. Illuminating Endosomal Escape of Polymorphic Lipid Nanoparticles That Boost mRNA Delivery. *Biomater. Sci.* **2021**, *9*, 4289−4300.
(21) Semple, S. C.; Akinc, A.; Chen, J.; Sandhu, A. P.; Mui, B. L.; Cho, C. K.; Sah, D. W. Y.; Stebbing, D.; Crosley, E. J.; Yaworski, E.; Hafez, I. M.; Dorkin, J. R.; Qin, J.; Lam, K.; Rajeev, K. G.; Wong, K. F.; Jeffs, L. B.; Nechev, L.; Eisenhardt, M. L.; Jayaraman, M.; et al. Rational Design of Cationic Lipids for siRNA Delivery. *Nat. Biotechnol.* **2010**, *28*, 172−176.
(22) Mui, B. L.; Tam, Y. K.; Jayaraman, M.; Ansell, S. M.; Du, X.; Tam, Y. Y. C.; Lin, P. J.; Chen, S.; Narayanannair, J. K.; Rajeev, K. G.; Manoharan, M.; Akinc, A.; Maier, M. A.; Cullis, P.; Madden, T. D.; Hope, M. J. Influence of Polyethylene Glycol Lipid Desorption Rates on Pharmacokinetics and Pharmacodynamics of siRNA Lipid Nanoparticles. *Mol. Ther.-Nucleic Acids* **2013**, *2*, No. e139.
(23) Mahmoudi, M.; Landry, M. P.; Moore, A.; Coreas, R. The Protein Corona from Nanomedicine to Environmental Science. *Nat. Rev. Mater.* **2023**, *8*, 422−438.
(24) Dilliard, S. A.; Sun, Y.; Brown, M. O.; Sung, Y.-C.; Chatterjee, S.; Farbiak, L.; Vaidya, A.; Lian, X.; Wang, X.; Lemoff, A.; Siegwart, D. J. The Interplay of Quaternary Ammonium Lipid Structure and Protein Corona on Lung-Specific mRNA Delivery by Selective Organ Targeting (SORT) Nanoparticles. *J. Controlled Release* **2023**, *361*, 361−372.
(25) Zhang, Z.; Guan, J.; Jiang, Z.; Yang, Y.; Liu, J.; Hua, W.; Mao, Y.; Li, C.; Lu, W.; Qian, J.; Zhan, C. Brain-Targeted Drug Delivery by Manipulating Protein Corona Functions. *Nat. Commun.* **2019**, *10*, 3561.
(26) Cai, R.; Chen, C. The Crown and the Scepter: Roles of the Protein Corona in Nanomedicine. *Adv. Mater.* **2019**, *31*, No. 1805740.
(27) Oh, J. Y.; Kim, H. S.; Palanikumar, L.; Go, E. M.; Jana, B.; Park, S. A.; Kim, H. Y.; Kim, K.; Seo, J. K.; Kwak, S. K.; Kim, C.; Kang, S.; Ryu, J. H. Cloaking Nanoparticles with Protein Corona Shield for Targeted Drug Delivery. *Nat. Commun.* **2018**, *9*, 4548.
(28) Cabral, H.; Li, J.; Miyata, K.; Kataoka, K. Controlling the Biodistribution and Clearance of Nanomedicines. *Nat. Rev. Bioeng.* **2023**, DOI: 10.1038/s44222-023-00138-1.
(29) Dilliard, S. A.; Cheng, Q.; Siegwart, D. J. On the Mechanism of Tissue-Specific MRNA Delivery by Selective Organ Targeting Nanoparticles. *Proc. Natl. Acad. Sci. U. S. A.* **2021**, *118*, No. e2109256118.
(30) Qiu, M.; Tang, Y.; Chen, J.; Muriph, R.; Ye, Z.; Huang, C.; Evans, J.; Henske, E. P.; Xu, Q. Lung-Selective mRNA Delivery of Synthetic Lipid Nanoparticles for the Treatment of Pulmonary Lymphangioleiomyomatosis. *Proc. Natl. Acad. Sci. U. S. A.* **2022**, *119*, No. e2116271119.
(31) Prapainop, K.; Witter, D. P.; Wentworth, P. A Chemical Approach for Cell-Specific Targeting of Nanomaterials: Small-Molecule-Initiated Misfolding of Nanoparticle Corona Proteins. *J. Am. Chem. Soc.* **2012**, *134*, 4100−4103.
(32) Yang, P.; Qin, H.; Li, Y.; Xiao, A.; Zheng, E.; Zeng, H.; Su, C.; Luo, X.; Lu, Q.; Liao, M.; Zhao, L.; Wei, L.; Varghese, Z.; Moorhead, J. F.; Chen, Y.; Ruan, X. Z. CD36-Mediated Metabolic Crosstalk between Tumor Cells and Macrophages Affects Liver Metastasis. *Nat. Commun.* **2022**, *13*, 5782.
(33) Nolasco, J.; Nolasco, L.; Da, Q.; Cirlos, S.; Ruggeri, Z.; Moake, J.; Cruz, M. Complement Component C3 Binds to the A3 Domain of von Willebrand Factor. *TH Open* **2018**, *2*, e338−e345.
(34) Frimat, M.; Tabarin, F.; Dimitrov, J. D.; Poitou, C.; Halbwachs-Mecarelli, L.; Fremeaux-Bacchi, V.; Roumenina, L. T. Complement Activation by Heme as a Secondary Hit for Atypical Hemolytic Uremic Syndrome. *Blood* **2013**, *122*, 282−292.
(35) Moein Moghimi, S.; Patel, H. M. Differential Properties of Organ-Specific Serum Opsonins for Liver and Spleen Macrophages. *Biochim. Biophys. Acta, Biomembr.* **1989**, *984*, 379−383.
(36) Nie, S. Understanding and Overcoming Major Barriers in Cancer Nanomedicine. *Nanomedicine (London, U. K.)* **2010**, *5*, 523−528.
(37) Raesch, S. S.; Tenzer, S.; Storck, W.; Rurainski, A.; Selzer, D.; Ruge, C. A.; Perez-Gil, J.; Schaefer, U. F.; Lehr, C. M. Proteomic and Lipidomic Analysis of Nanoparticle Corona upon Contact with Lung Surfactant Reveals Differences in Protein, but Not Lipid Composition. *ACS Nano* **2015**, *9*, 11872−11885.
(38) Blanco, E.; Shen, H.; Ferrari, M. Principles of Nanoparticle Design for Overcoming Biological Barriers to Drug Delivery. *Nat. Biotechnol.* **2015**, *33*, 941−951.
(39) Kim, J.; Eygeris, Y.; Ryals, R. C.; Jozić, A.; Sahay, G. Strategies for Non-Viral Vectors Targeting Organs beyond the Liver. *Nat. Nanotechnol.* **2023**, DOI: 10.1038/s41565-023-01563-4.
(40) Toya, S. P.; Malik, A. B. Role of Endothelial Injury in Disease Mechanisms and Contribution of Progenitor Cells in Mediating Endothelial Repair. *Immunobiology* **2012**, *217*, 569−580.
(41) Li, Y. X.; Wang, H. B.; Li, J.; Jin, J. B.; Hu, J. B.; Yang, C. L. Targeting Pulmonary Vascular Endothelial Cells for the Treatment of Respiratory Diseases. *Front. Pharmacol.* **2022**, *13*, No. 983816.
(42) Danos, O.; Van, E. S.; Yoo, J.; Patel, S.; Ghanekar, A.; O'berry, A.; Irwin-Pack, K.; Curtiss, D. Gene Therapy For Eye Pathologies. WO 2020/206098 A1, 2020.
(43) Tozinameran. Global Substance Registration System (GSRS). National Center for Advancing Translational Sciences (NCATS). n.d. https://gsrs.ncats.nih.gov/ginas/ (accessed 2024−02−22; FDA UNII: 5085ZFP6SJ).
(44) Haryadi, R.; Ho, S.; Kok, Y. J.; Pu, H. X.; Zheng, L.; Pereira, N. A.; Li, B.; Bi, X.; Goh, L. T.; Yang, Y.; Song, Z. Optimization of Heavy Chain and Light Chain Signal Peptides for High Level Expression of Therapeutic Antibodies in CHO Cells. *PLoS One* **2015**, *10*, No. e0116878.
(45) Feige, M. J.; Groscurth, S.; Marcinowski, M.; Shimizu, Y.; Kessler, H.; Hendershot, L. M.; Buchner, J. An Unfolded CH1 Domain Controls the Assembly and Secretion of IgG Antibodies. *Mol. Cell* **2009**, *34*, 569−579.
(46) Leitzgen, K.; Knittler, M. R.; Haas, I. G. Assembly of Immunoglobulin Light Chains as a Prerequisite for Secretion: A Model for Oligomerization-Dependent Subunit Folding. *J. Biol. Chem.* **1997**, *272*, 3117−3123.
(47) Karikó, K.; Muramatsu, H.; Welsh, F. A.; Ludwig, J.; Kato, H.; Akira, S.; Weissman, D. Incorporation of Pseudouridine into mRNA Yields Superior Nonimmunogenic Vector with Increased Translational Capacity and Biological Stability. *Mol. Ther.* **2008**, *16*, 1833−1840.
(48) Luong, R. H. The Laboratory Mouse. In *The Clinical Chemistry of Laboratory Animals*, 3rd ed.; Kurtz, D. M., Travlos, G. S., Eds.; CRC Press: Boca Raton, FL, 2017; pp 24−27. DOI: 10.1201/9781315155807.
(49) Santiago-Cardona, P. G. *Lung Cancer: Methods and Protocols*, 1st ed.; Humana Press, 2021. DOI: 10.1007/978-1-0716-1278-1.
(50) Bressenot, A.; Marchal, S.; Bezdetnaya, L.; Garrier, J.; Guillemin, F.; Plénat, F. Assessment of Apoptosis by Immunohistochemistry to Active Caspase-3, Active Caspase-7, or Cleaved PARP in Monolayer Cells and Spheroid and Subcutaneous Xenografts of Human Carcinoma. *J. Histochem. Cytochem.* **2009**, *57*, 289−300.

(51) Sun, X.; Kaufman, P. D. Ki-67: More than a Proliferation Marker. *Chromosoma* **2018**, *127*, 175−186.
(52) Keith, B.; Simon, M. C. Tumor Angiogenesis. In *The Molecular Basis of Cancer*, 4th ed.; Mendelsohn, J., Howley, P. M., Israel, M. A., Gray, J. W., Thompson, C. B., Eds.; Saunders: China, 2015; pp 257−268. DOI: 10.1016/B978-1-4557-4066-6.00017-2.
(53) Mordant, P.; Loriot, Y.; Lahon, B.; Castier, Y.; Lesèche, G.; Soria, J. C.; Vozenin, M. C.; Decraene, C.; Deutsch, E. Bioluminescent Orthotopic Mouse Models of Human Localized Non-Small Cell Lung Cancer: Feasibility and Identification of Circulating Tumour Cells. *PLoS One* **2011**, *6*, No. e26073.
(54) Matsumoto, S.; Tanaka, F.; Sato, K.; Kimura, S.; Maekawa, T.; Hasegawa, S.; Wada, H. Monitoring with a Non-Invasive Bioluminescent in Vivo Imaging System of Pleural Metastasis of Lung Carcinoma. *Lung Cancer* **2009**, *66*, 75−79.
(55) Rohner, E.; Yang, R.; Foo, K. S.; Goedel, A.; Chien, K. R. Unlocking the Promise of mRNA Therapeutics. *Nat. Biotechnol.* **2022**, *40*, 1586−1600.
(56) Rojas; Sethna, L. A.; Soares, Z.; Olcese, K. C.; Pang, C.; Patterson, N.; Lihm, E.; Ceglia, J.; Guasp, N.; Chu, P.; Yu, A.; Chandra, R.; Waters, A. K.; Ruan, T.; Amisaki, J.; Zebboudj, M.; Odgerel, A.; Payne, Z.; Derhovanessian, G.; Müller, E.; et al. Personalized RNA Neoantigen Vaccines Stimulate T Cells in Pancreatic Cancer. *Nature* **2023**, *618*, 144−150.
(57) Kim, M.; Jeong, M.; Hur, S.; Cho, Y.; Park, J.; Jung, H.; Seo, Y.; Woo, H. A.; Nam, K. T.; Lee, K.; Lee, H. Engineered Ionizable Lipid Nanoparticles for Targeted Delivery of RNA Therapeutics into Different Types of Cells in the Liver. *Sci. Adv.* **2021**, *7*, No. eabf4398.
(58) Cheng, Q.; Wei, T.; Farbiak, L.; Johnson, L. T.; Dilliard, S. A.; Siegwart, D. J. Selective Organ Targeting (SORT) Nanoparticles for Tissue-Specific mRNA Delivery and CRISPR−Cas Gene Editing. *Nat. Nanotechnol.* **2020**, *15*, 313−320.
(59) Kim, J.; Jozic, A.; Mukherjee, A.; Nelson, D.; Chiem, K.; Khan, M. S. R.; Torrelles, J. B.; Martinez-Sobrido, L.; Sahay, G. Rapid Generation of Circulating and Mucosal Decoy Human ACE2 Using mRNA Nanotherapeutics for the Potential Treatment of SARS-CoV-2. *Adv. Sci.* **2022**, *9*, No. 2202556.
(60) Huang, C.; Duan, X.; Wang, J.; Tian, Q.; Ren, Y.; Chen, K.; Zhang, Z.; Li, Y.; Feng, Y.; Zhong, K.; Wang, Y.; Zhou, L.; Guo, G.; Song, X.; Tong, A. Lipid Nanoparticle Delivery System for mRNA Encoding B7H3-Redirected Bispecific Antibody Displays Potent Antitumor Effects on Malignant Tumors. *Adv. Sci.* **2023**, *10*, No. 2205532.
(61) Deng, Y. Q.; Zhang, N. N.; Zhang, Y. F.; Zhong, X.; Xu, S.; Qiu, H. Y.; Wang, T. C.; Zhao, H.; Zhou, C.; Zu, S. L.; Chen, Q.; Cao, T. S.; Ye, Q.; Chi, H.; Duan, X. H.; Lin, D. D.; Zhang, X. J.; Xie, L. Z.; Gao, Y. W.; Ying, B.; Qin, C. F. Lipid Nanoparticle-Encapsulated mRNA Antibody Provides Long-Term Protection against SARS-CoV-2 in Mice and Hamsters. *Cell Res.* **2022**, *32*, 375−382.
(62) Rui, Y.; Wilson, D. R.; Tzeng, S. Y.; Yamagata, H. M.; Sudhakar, D.; Conge, M.; Berlinicke, C. A.; Zack, D. J.; Tuesca, A.; Green, J. J. High-Throughput and High-Content Bioassay Enables Tuning of Polyester Nanoparticles for Cellular Uptake, Endosomal Escape, and Systemic in Vivo Delivery of mRNA. *Sci. Adv.* **2022**, *8*, No. eabk2855.
(63) Nguyen, H. T.; Phung, C. D.; Tran, T. H.; Pham, T. T.; Pham, L. M.; Nguyen, T. T.; Jeong, J. H.; Choi, H. G.; Ku, S. K.; Yong, C. S.; Kim, J. O. Manipulating Immune System Using Nanoparticles for an Effective Cancer Treatment: Combination of Targeted Therapy and Checkpoint Blockage miRNA. *J. Controlled Release* **2021**, *329*, 524−537.
(64) Lee, Y. H.; Andersen, J. B.; Song, H. T.; Judge, A. D.; Seo, D.; Ishikawa, T.; Marquardt, J. U.; Kitade, M.; Durkin, M. E.; Raggi, C.; Woo, H. G.; Conner, E. A.; Avital, I.; MacLachlan, I.; Factor, V. M.; Thorgeirsson, S. S. Definition of Ubiquitination Modulator COP1 as a Novel Therapeutic Target in Human Hepatocellular Carcinoma. *Cancer Res.* **2010**, *70*, 8264−8269.
(65) Rybakova, Y.; Kowalski, P. S.; Huang, Y.; Gonzalez, J. T.; Heartlein, M. W.; DeRosa, F.; Delcassian, D.; Anderson, D. G. mRNA Delivery for Therapeutic Anti-HER2 Antibody Expression In Vivo. *Mol. Ther.* **2019**, *27*, 1415−1423.
(66) Suchowski, K.; Pöschinger, T.; Rehemtulla, A.; Stürzl, M.; Scheuer, W. Noninvasive Bioluminescence Imaging of AKT Kinase Activity in Subcutaneous and Orthotopic NSCLC Xenografts: Correlation of AKT Activity with Tumor Growth Kinetics. *Neoplasia (N. Y., NY, U. S.)* **2017**, *19*, 310−320.
(67) Yu, F.; Wang, X.; Guo, Z. S.; Bartlett, D. L.; Gottschalk, S. M.; Song, X. T. T-Cell Engager-Armed Oncolytic Vaccinia Virus Significantly Enhances Antitumor Therapy. *Mol. Ther.* **2014**, *22*, 102−111.

https://doi.org/10.1021/acsnano.3c13039
ACS Nano 2024, 18, 8392−8410